Characterization of Methane Based Graphene Synthesis on H13 Tool Steel

by

Thibankumar A/L Arumugam
15956

Dissertation submitted in partial fulfilment of
the requirements for the
Bachelor of Engineering (Hons)
(Mechanical)

JANUARY 2016

Universiti Teknologi PETRONAS
Bandar Seri Iskandar
32610 Tronoh
Perak Darul Ridzuan

TABLE OF CONTENTS

LIST OF FIGURES

LIST OF TABLES

CERTIFICATION OF APPROVAL

Characterization of Methane Based Graphene Synthesis on H13 Tool Steel

by

Thibankumar A/L Arumugam
15956

A project dissertation submitted to the
Mechanical Engineering Programme
Universiti Teknologi PETRONAS
in partial fulfilment of the requirement for the
BACHELOR OF ENGINEERING (Hons)
(MECHANICAL)

Approved by,

_____

(A.P. Ir. Dr. Mokhtar Bin Awang)

UNIVERSITI TEKNOLOGI PETRONAS
TRONOH, PERAK
January 2016

CERTIFICATION OF ORIGINALITY

This is to certify that I am responsible for the work submitted in this project, that the original work is my own except as specified in the references and acknowledgements, and that the original work contained herein have not been undertaken or done by unspecified sources or persons.

_____

THIBANKUMAR A/L ARUMUGAM

ABSTRACT

As the demand to weld higher strength materials through friction stir welding increases, the need for better non-consumable rotating tool increases as it has to be able to endure high frictional and thermal deformation while the workpiece undergoes intense plastic deformation at high temperatures. This project aims to make use of graphene (Young's Modulus = 1.0 TPa) in the improvement of friction stir welding tools. Nickel is coated on H13 Tool Steel substrate via Magnetron Sputtering to act as a catalyst for graphene growth. Graphene synthesis with methane gas is done through Chemical Vapour Deposition (CVD) process. Characterization of the interface layers are done with Raman Spectroscopy, X-ray Photoelectron Spectroscopy, Field Emission Scanning Electron Microscope, and Energy Dispersive Spectroscopy. In this report, characterisation experiments revealed an absence of graphene on bare substrate as well as the allegedly nickel coated substrate. Analysis of the surface elements revealed no nickel coating which is inferred to be the main cause of the absence of graphene. Interestingly, FE-SEM revealed crystal like structure and graphitic is nature as determined by XPS and EDS techniques.

Keywords: Friction stir welding, graphene, chemical vapour deposition, Raman spectroscopy, x-ray photoelectron spectroscopy (XPS), field-emission scanning electron microscope (FE-SEM), energy dispersive spectroscopy (EDS)

ACKNOWLEDGEMENT

Prima facie, I am grateful to the God for the good health and wellbeing that were necessary to complete this dissertation. Though only my name appears on the cover of this dissertation, a great many people have contributed to its production. I owe my gratitude to all those people who have made this dissertation possible and because of whom my graduate experience has been one that I will cherish forever.

My deepest gratitude is to my supervisor, AP Ir. Dr. Mokhtar Awang. I have been amazingly fortunate to have a supervisor who gave me the freedom to explore on my own, and at the same time the guidance to recover when my steps faltered. His patience and support helped me overcome many crisis situations and finish this dissertation. I am also thankful to him for encouraging the use of correct grammar and consistent notation in my writings and for carefully reading and commenting on countless revisions of this dissertation.

I would like to thank my co-supervisor, AP Dr. Patthi Hussain, who has always been there to listen and give advice. I am deeply grateful to him for the long discussions that helped me sort out the technical details of my work.

I would like to thank Prof. Dr. Norani Muti, Dr. Mohamed Shuaib Mohamed Saheed, and Mr. Rosli of UTP Centre of Innovative Nanostructure & Nanodevices (COINN) for the advices and sharing their technical expertise in conducting experiments and necessary lab works in regard to this this project.

Finally, I would like to express my gratitude to Mr. Sattar Emamian for his guidance throughout the project especially in conducting experiments and analysing results. Him sharing his knowledge regarding this project allowed for better understanding of data obtained from experiments that were conducted.

I take this opportunity to express gratitude to all the members of the Mechanical Engineering Department for their help and support. I also thank my family and friends for the unceasing encouragement, support and attention.

CHAPTER 1
INTRODUCTION

1.1 Background Study

In 1991, an English company called The Welding Institute (TWI) developed the world's first friction stir welding (FSW) [1] [2]. With this development, difficult welds could be completed with an end result of significant quality. Friction stir welding (FSW) is a solid state joining process that makes use of a non-consumable rotating tool in order to join two facing surfaces by traversing along the joint line. FSW uses a milling machine due to similar movement conditions but instead of the typical milling tool, a specific non-consumable rotating tool is used. It is important to note that since FSW is a solid state joining process, the welded metal does not undergo melting, hence making it particularly energy efficient in comparison to conventional welding techniques. In addition to that, FSW is considered to be environmentally friendly due to zero flux or cover gas usage. FSW is often implemented when conventional welding techniques produce undesired outcome, mainly due to poor porosity and solidification microstructure in the weld fusion zone. Furthermore, its ability to join metals regardless of its composition compatibility proves its versatility [2].

One of the main components of the FSW is the non-consumable rotating tool. A non-consumable rotating tool consist of a specifically designed shoulder and pin which is inserted into the adjacent edges of the plates to be welded and is allowed to traverse along the joint line [1] [2]. The tool serves three critical functions which are to heat the workpiece by means of friction, displace the workpiece materials to produce the joint, and to ensure the containment of hot metal beneath the tool shoulder [2] [3]. Due to this, the performance of the tool influences the end product of the solid-state joint.

The current design of the non-consumable rotating tool allows workpiece material thickness ranging from 0.5mm up till 65mm to be welded from one side of the surface at full penetration without any issues involving porosity or internal voids. In regard to material of the workpiece, non-ferrous alloys are most commonly used. This is largely because of limitation caused by the non-consumable rotating tool which tend to be manufactured from hardened ferrous alloys. These hardened ferrous alloys tools are preferred due to their high machinability, and excellent thermal, and wear resistance especially when used with aluminium and copper workpieces [3].

Friction stir welding utilizes the thermomechanical deformation process in which the tool's temperature approaches the solidus temperature of the workpiece material [3] [4]. In the initial stages of the plunge, heat is released due to the friction of the non-consumable rotating tool's pin and the workpiece. After the plunging stage, the shoulder of the non-consumable rotating tool makes contact with the workpiece. This contact relates to highest heat component liberation [3]. The frictional and deformational heating caused by the tool must only affect the workpiece and never the FSW tool. Any FSW tool will undergo high abrasive wear, as well as constant high ranges of temperature and dynamic effects [3]. Thus, it is very important that the tool has very good wear resistance, high temperature strength and temper resistance, as well as good toughness. In order to produce a proper solid-state joint through friction stir welding, suitable tool material selection based on the desired workpiece. Some of the material characteristics that has to be considered during tool design are the ambient and elevated temperature strength, elevated temperature stability, tool reactivity, wear resistance, fracture toughness, coefficient of thermal expansion, and machinability [3] [4].

1.2 Problem Statement

Metals such as steel and aluminium have been widely used in various fields such as ship constructions, and space industries. Amongst both metals, aluminium has been found to be more practical for the application of friction stir welding (FSW). This is because the melting point of steel is relatively high, thus requiring non-consumable rotating tools of excellent properties at elevated temperatures. Since the type of material of the tool co-relates to the type of material of the workpiece, the tool has to

be able to withstand the frictional and deformational heating while the workpiece undergoes intense plastic deformation at high temperatures.

Tools manufactured from polycrystalline cubic boron nitride (PCBN) have been introduced due to its excellent mechanical properties especially in terms of mechanical strength and thermal resistivity. However, the cost of manufacturing this tool, and well as poor machinability poses a hurdle in its practical usage. It is believed that the introduction of graphene in the manufacturing of the tool would allow for solid state joining of high strength metals with a reduced wear rate. In addition to that, process of synthesizing graphene is relatively economical and its excellent bending abilities allow for excellent tool machinability. Finally, a research gap exists especially towards coating of graphene on H13 tool steel where the coating techniques of graphene on this alloy has not been fully studied to allow for further advancement of graphene coating to improve its mechanical properties.

1.3 Objectives

This project aims to study the synthesizing ability graphene through chemical vapour deposition by pyrolysis of methane gas on H13 tool steel. Through this study, the research gap that exist in synthesizing graphene on H13 tool steel may be narrowed. With the results obtained in the study, future studies on the improvement on graphene synthesizing method as well as mechanical properties of the graphene coating may be conducted. The key objectives of this project are:

1. To characterize surface structure of graphene synthesized through chemical vapour deposition by pyrolysis of methane gas on H13 tool steel.
2. To study the effect of heat-treatment of H13 tool steel on graphene synthesized through chemical vapour deposition by pyrolysis of methane gas.

Throughout this project, testing and relevant studies would be carried out towards achieving all the points mentioned above to prove or disprove that a viable solution is indeed possible to be conceived when it comes to synthesizing graphene on H13 tool steel.

1.4 Scope of Study

This study focuses on synthesizing graphene on a friction stir welding tool (FSW) fabricated from H13 tool steel. The nickel coating that would act as the catalyst for graphene synthesis would be coating via sputtering process. The graphene layer on nickel would be synthesized through the process of chemical vapour deposition (CVD) by methane pyrolysis. The results obtained would characterize the surface structure of graphene synthesized as well as the effect of heat treatment on graphene synthesis.

CHAPTER 2
LITERATURE REVIEW

The non-consumable rotating tool of a friction stir welding (FSW) is one of the most critical component in ensuring proper solid state joining of workpiece. Material selection for the tool is an important criterion in which it determines the type workpiece material that can be welded, life expectancy of the tool, and the overall user experience [3]. This is because the tool has to be able to retain its dimensional stability and design features when approaching the workpiece's solidus temperature through the process of thermomechanical deformation [4]. Some of the important characteristics that has to be considered for tool material selection are the ambient-and-elevated-temperature strength, elevated-temperature stability, wear resistance, tool reactivity, fracture toughness, coefficient of thermal expansion, machinability, uniformity in density and microstructure, and material availability [3] [4].

2.1 Common FSW Tool Materials

One of the most common type of tool material is hot-worked tool steel. This is due to the fact that hot-worked tool steel is easy to be obtained and machined, as well as being a low cost. AISI H13 which is a chromium-molybdenum hot-worked, air hardened steel is a common tool material for FSW due to its exhibition of tremendous wear, fatigue and thermal resistance, plus excellent elevated elevated-temperature strength when coupled with workpiece of aluminium alloys [3] [4] [5]. H13 has been shown to be able to weld copper of thickness up to 3mm but tool degradation was observed at copper thickness of 10mm. It also undergoes high tool wear rate when applied with workpiece of high metal strength [5]. Based on ASTM A681, the hardness value for hot-worked tool steel ranges from 28 to 53 HRC, depending on the tempered temperature [6].

Nickel- and cobalt-base alloys, originally made for the manufacturing of aircraft engine components proved to be a viable source of material for FSW tools due to its high strength, ductility, hardness stability, creep resistance, and material availability [3] [4] [5]. Metal alloys such as IN738LC, Stellite 12, Nimonic 90, and Waspalloy have been used as the tool material for applications that involve various copper alloys [4]. These alloys derive their strength heavily from precipitation hardening thus tool operating temperature should always be below their precipitation temperature which is normally between 600°C and 800°C [3]. However, due to their high strength, nickel- and cobalt-base alloys tend to have very low machinability thus causing difficulty in designing the tool features [4]. These alloys, especially nickel-based alloys have hardness ranging from as low as 30 HRC to 42 HRC [7].

Refractory metals such as molybdenum and niobium are often used as tool material due to their ability to endure high working temperatures which is around 1000°C to 1500°C which is suitable in copper-alloy solid-state joining. The downsides in using refractory metals are their lack of availability and poor machinability, as well as reduced tool fracture toughness (increase in brittleness) whenever powder processed tools are involved [4]. Tungsten based metals are common refractory metals used for FSW tools. Tungsten-rhenium has high working temperature but has poor machinability. To improve machinability, Densimet (nickel-iron-tungsten alloy) which is a more economical option was introduced in the expense of high working temperature [4]. Densimet has been measured to have a hardness of 34 HRC [8].

Metals reinforced with carbide particles are used due to excellent wear resistance, and acceptable fracture toughness [4]. There are reports of tool failure in the plunging stage with tools for carbide reinforced metals as well as excessive wear rates on FSW tools with threads [4] [5]. Recently, FSW tools made from polycrystalline cubic boron nitride (PCBN) and polycrystalline diamond (PCD) has been widely used for workpieces with ultra-high strength and working temperature such as titanium and other exotic alloys. These tools are called super abrasive tools due to presence of ultra-hard crystals in the material's matrix [4] [5] [9]. The Knoop harness of cutting tool PCBN has been reported to be at 39 GPa [10]. Widespread application of this material has been hindered by high tool making cost due to extreme manufacturing processes, poor toughness and machinability. In addition to that, PCBN tools are only suitable for

tools with low levels of spindle eccentricity, thus reducing its versatility in common FSW applications [4].

2.2 Introduction to Graphene

Graphene is a single layer of carbon atom densely packed into a hexagonal crystal lattice. It is one atomic thick consisting of hybrid sp^2 bonds. It is important to note that there are several types of graphene sheets; single layer, bi-layer, and multilayer in which the number of graphene layers must be less or equal to 10 [11]. Graphene has become more prominent in the engineering field due to its extraordinary mechanic properties that exceed that of any other known materials. With this knowledge, there is a high possibility of manufacturing FSW tools with graphene.

A computer simulated study has been conducted using ab initio to determine the ideal tensile strength of flat graphene. The ideal strength of a crystal lattice is related to its phonon where the phonon's instability relates to crystal's mechanical instability. This condition is then mathematical related to the Cauchy-Born rules relating to the stress-strain [12]. Density functional perturbation theory (DFPT) is an ab initio method that is used to obtain accurate phonon calculations thus the ability to determine phonon instability. When a free surface in applied a certain amount of load, the surface ideal strength can be calculated from the analysis of the surface phonon. In the case of graphene, uniaxial stress is applied in the x and y direction causing a zig-zag and armchair tensile deformation [12]. The changes in the phonon's stability is translated to ideal strain and strength using the afro-mentioned Cauchy-Born rules. The results obtained for the Young's Modulus, E is 1.05 TPa with a Poisson's ratio of 0.186. In addition to that, the intrinsic stress value obtained from the zig-zag deformation is 110 GPa [12].

An experiment conducted using AFM nano-indentation technique where nano-indentation was done on a layer of suspended monolayer graphene (thickness 0.335 nm) proved that the high mechanical properties of graphene. The results show that the intrinsic strength value of graphene is 42 ± 4 Nm^{-1} which corresponds to the Young's modulus of $E = 1.0 \pm 0.1$ TPa, and a third order elastic stiffness of $D = -2.0 \pm 0.4$ TPa [14]. In addition to that, an intrinsic stress value of 130 ± 10 GPa at an intrinsic strain

value of 0.25 shows a brittle fracture that corresponds to the highest value ever obtained for any real material [14]. Comparing these values to the simulation experimental where the Young's modulus is 1.05 TPa, and the intrinsic stress value is 110 GPa show a very close relation between both values [12]. These values are found to be extremely large thus makes graphene an extremely viable choice for applications that require high strength. The mechanical properties of graphene are very much controlled by the crystal lattice microstructure as well as the defects [13]. It is known that lattice geometry governs the elastic properties where else the defects affects the strength and plastic flow stresses [14]. Since graphene is present in a micro-scaled environment, defects free crystal lattices can be grown through controlled synthesis.

2.3 Nickel as a Catalyst for Graphene Synthesis

Since graphene has been proven to be a viable option in engineering and industrial application, suitable metal catalyst has to be selected to ensure defect free graphene synthesis. Various transition metals have been used as a substrate in the growth of graphene due to the metals' ability to segregate into graphite onto their surfaces upon cooling [15]. Transition metal, nickel, has been proven to be one of the most viable substrate for graphene growth based on its catalytic abilities such that it is able to dehydrogenate hydrocarbons precursors with ease and consequently allows for proper formation of hexagonal (honey comb) crystal lattice of graphene [16]. An important point to note is that, the crystal structure of nickel has to be in ‹111› orientation for a perfectly epitaxial formation of hexagonal latticed monolayer graphite [17].

Carbon solubility of metals determine whether graphene grows at the surface, as it is for the case of copper, carbon is deposited on top of it while in the case of nickel, carbon dissolves. Metals with high amount of carbon solubility has equally high ability to precipitate carbon upon cooling to form multi-layers of graphene [18]. Based on the Table 2.1, relative to the metals listed, nickel has the fourth highest solubility of carbon. A relatively high carbon solubility in comparison to copper allows for a low precursor operating pressure and temperature for the growth of monolayer graphene [18].

Table 2.1: Solubility of carbon in various transition metals at 1000°C [18].

Transition Metal	Solubility of carbon (% atom) at 1000°C
Copper (Cu)	0.04
Ruthenium (Ru)	1.56
Nickel (Ni)	2.03
Cobalt (Co)	3.41
Rhenium (Re)	4.39
Palladium (Pd)	5.98

Graphene-metal separation which depends on the moiré patterns is equally important in the determination of the graphene-metal interaction strength. A lack of moiré pattern proves that there is a very close lattice match between nickel and graphene (approximately 1% of mismatch). Due to this close lattice match, the separation between graphene and nickel is minimal thus allowing for better formation of epitaxial graphene layers [16]. Based on measurements, nickel has been found to have a separation of 0.21 nm which is consistent with metals that have a strong interaction with graphene [18]. This evidence concurs with density functional theory (DFT) analysis where the 'fcc' configuration of nickel is the strongest and most stable adsorption site, with an adhesion work of 0.81 Jm^{-2} [18].

2.4 Deposition of Nickel on Tool Steel

From the paragraphs above, it has been proven that nickel is very suitable and important for the growth of graphene. This project mainly focusses on FSW tools; the most common material selection for it is tool steel. Hence, for this project to be viable, the tool steel has to be coated with nickel. Many methods of nickel depositions are available, for example, chemical vapour deposition, electroplating, and physical vapour deposition. Deposition of nickel via magnetron sputtering have shown very good corrosion as well as wear resistance especially on steel substrates. With the use of magnetron sputtering, the atomic crystal structure can be controlled through parametric settings. In addition to that, the thickness of the nickel deposited can be controlled by determining the deposition rate based on set parameters [19].

2.5 Synthesis of Graphene on Nickel

There are several methods in synthesizing epitaxial graphene on nickel: segregation of carbon from nickel to its surface, physical vapour deposition, and CVD of hydrocarbons [20]. CVD is often favoured for growth of graphene due to its high manufacturing potential. Another advantage of CVD is that it allows for the use of nickel as a catalyst in the deposition of graphene on the metal substrate [16]. Essentially, CVD is a process of depositing thin solid films on a given substrate from a vapour species by the means of chemical reactions. The main section of CVD is the reactor as it is responsible for containing the chemical reactions that ensures the depositions of precursors on the metal substrate (nickel). The temperature, pressure and duration of precursor in the reaction are closely monitored as well. Besides those parameters, boundary conditions above substrate, pyrolysis rate, number of intermediate steps for precursors decomposition, grain boundary condition of substrate, presence of catalyst, and rate of reaction play an equally important role in the synthesis of graphene through the process of CVD [21].

In CVD process, impact of nickel as a catalyst is quite predominant in ensuring a heterogeneous reaction where precursor decomposes onto the surface of the substrate. The nickel substrate which acts as a catalyst prevents the gaseous precipitation of carbon clusters which would eventually form soot and place themselves on synthesized graphene [21]. Furthermore, the nickel catalyst lowers the energy barrier required for the reaction which in turn allows for the formation of graphene through decomposition of precursors at a significantly lower temperature. This proves that nickel catalysts allow for a more controlled rate of reaction in a CVD process [18] [21].

Although CVD and nickel seem to be the perfect match for the synthesis of graphene, there are several challenges involved. Firstly, the rate of precipitation of carbon from nickel upon cooling is difficult to be controlled, thus effecting the thickness of the graphene deposited on the surface. In addition to that, the surface of the substrate (nickel) has to be defect free as precipitating carbon tend to gather at location with higher surface energy (e.g. surface trenches, grain boundaries) [18] [21]. Gathering of precipitated carbon at these locations cause uneven formation of monolayer graphene. Besides that, due to poor understanding of the intermediate steps of precursor's

pyrolysis, the rate of carbon supply is relatively tough to be controlled. This is because higher number of intermediate steps of a precursor's pyrolysis causes an increase in freedom of carbon supply [21]. This is an unwanted trait in the formation of graphene as the purpose is to control the amount of carbon interacting with the substrate.

2.6 Verification of Synthesized Graphene

2.6.1 Raman Spectroscopy

Raman spectroscopy allows for the determination and verification of graphene growth. This is because Raman spectra is able to provide the characteristic peaks of graphene. These peaks are the D peak, G peak, and 2D peak. The D peak which occurs at ~1350cm^{-1} signifies that the synthesized graphene contains disorders and defects. It has been reported that these might have occurred due to surface dislocations, corrugation, and possibly the interaction of graphene with the substrate itself [22]. Meanwhile, the G peak that occurs at ~1580cm^{-1} which is due to the in-plane vibration of sp^2 carbon atoms. Finally, the 2D peak occurs at ~2675cm^{-1} which is due to the stacking order of graphene sheets [23].

Synthesis of graphene may be categorized into single layer graphene (SLG) and multi-layer graphene (MLG). This categorization can be determined through the intensity of the aforementioned D, G, and 2D peaks. For SLG and MLG, the presence of D peak is common as defects are easily formed on few layer graphene in comparison to graphite (more than 10 layers of graphene) although graphene synthesis without any defects has been done and reported even with nickel catalyst [24] [25]. The distinct contrast between SLG and MLG is the intensity of G and 2D peaks. For the case of SLG, the 2D peak would be approximately 4 times the intensity of the G peak. This would result in an G peak and 2D peak intensity ratio (I_G/I_{2D}) of approximately 0.25 [24] [26] [27]. In the case of MLG however, the 2D peak would be of lower intensity relative to G peak. This is because an increase number of carbon atom would result in a higher in-plane vibration of sp^2 carbon atoms [26] [27]. Therefore, with a higher G peak intensity, the I_G/I_{2D} ratio would be significantly greater than 0.25. This is backed up my experiments where I_G/I_{2D} ratio of greater than 1.0 has been reported for MLG

[28] [27]. In addition to this, an asymmetrical peak of either the G or 2D is characteristic of MLG as well [22] [29].

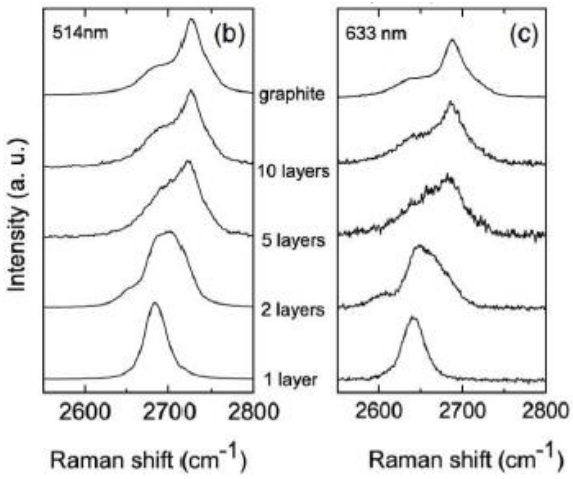

Figure 2.1: 2D-band peaks of Raman spectra in correlation to the thickness of deposited graphene and the number of graphene layers [21].

2.6.2 X-Ray Photoelectron Spectroscopy

X-Ray Photoelectron Spectroscopy is often used to determine the type of carbon bonds after the process of graphene synthesis. Graphitic structures with graphitic carbon-carbon (C-C) bond are represented by a significant peak at a binding energy of ~284eV to ~285eV [30]. This range of binding energy is characteristic of covalent sp2 hybridized carbon which validates the presence of graphene. An addition validation is that the presence of a peak at binding energy between of ~284eV to ~285eV gives the confirmation that the C-C bond are arranged in a hexagonal lattice structure [23] [29] [30].

2.7 Interface Properties

2.7.1 Graphene and Nickel Interface Adhesion Energy

Through research, it has been found that graphene-metal interfaces have properties such as strength, and cohesive energy that directly correlates to their atomic geometry [31]. The properties of graphene-nickel interface have been often compared with graphene-copper interface due to their very distinct graphitization methods, the former

being through precipitation of carbon, and the latter being through deposition of carbon [21]. Generally, it is known that copper has a weak cohesion with graphene in comparison to nickel. The structure and properties of these hybrid systems are studied using local density approximation (LDA). It has been determined that the stacking geometry between graphene and metals affect the cohesion levels and binding energies [31].

At a distance of 2.24 Å between the graphene and metal interface, copper has a binding energy, $E_{b(copper)}$ of -24.81 meV Å^{-2} while nickel has a binding energy, $E_{b(nickel)}$ of -91.33 meV Å^{-2}. Even with optimized top-fcc structure, nickel has shown a much closer distance between the graphene at 2.018 Å in comparison to copper at 2.03 Å. The graphene-nickel interface distance is very close to the interlayer distance of graphene which is at 2.03 Å. A tensile test analysis of the graphene-metal interface show that graphene-nickel interface has a tensile strength of 18.70 GPa while graphene-copper interface has a mere 2.92 GPa [31].

Further research was done using nano-scratch technique where a lateral force is used to remove the graphene layer off the metal substrate. It is to note that forces to de-bond graphene may vary due to grain boundaries, presence of different grains, and interlayer slippage of graphene. By plotting a force-displacement diagram, the area under the curve is obtained as the de-bonding energy, also known as the adhesion energy. Based on table 2.2, the adhesion energy per unit area of the graphene-nickel interface is approximately 6 times higher than of graphene-copper [32].

Table 2.2: Comparison of the adhesion energy per unit area between nickel and copper [32].

	Graphene-Copper	**Graphene Nickel**
Scratch area	44.16 mm^2	3.60 mm^2
Interfacial energy	563.14 pJ	261.75 pJ
Energy per unit area	12.75 Jm^{-2}	72.70 Jm^{-2}

To support the obtained adhesion energy, density functional theory (DFT) was applied to determine to calculate the chemical bonding state, which in turn allows to determine

the bond overlap population (BOP) and the net charge migration (NetC) of the graphene-metal interface. Interpretation of BOP and NetC values allows for a good estimation of the bond strength between two interfaces. From the experiment, a higher value of BOP was obtained for nickel in comparison to copper. This proves that larger number of electrons are shared between nickel and carbon atoms, thus having a stronger adhesion energy. Aside of that, the NetC values further justifies the interfacial strength of nickel and graphene where nickel has a slower rate of net charge migration when the interfacial distance is increased [32].

2.7.2 Hardness of H13 Steel-Nickel Interface

As stated by [33], the hardness of a H13 tool steel has been measured to have a hardness range of 48.0 to 50.0 HRC. This is consistent with the formation of strong and hard martensite grains. In addition to that, annealed H13 tool steel has been measured to have a HRC value of under 20. Since the nickel coating on the H13 tool steel is electroless, it has been reported that electroless nickel coating have a Knoop micro-hardness value ranging from 500 to 720. The micro-hardness value depends on the phosphorous content where higher phosphorous content allows for a greater micro-hardness. An experiment to determine the strength of the interface between electroplated steel and low carbon steel substrate was conducted. From that experiment, it has been determined that the interfacial strength increases as the thickness of nickel coating increases. It was determined that the adhesion energy for nickel coating with a thickness of 15 µm is 296.86 Jm^{-2} while nickel coating with a thickness of 25 µm has a much greater adhesion energy of 269.40 Jm^{-2} [34].

2.7.3 Hardness of Graphene-Nickel Interface

Much has not been researched on the hardness of graphene interface. However, the adhesion strength of graphene grown on nickel has been compared with graphene grown on copper. In this scenario, graphene grown on nickel has been proven to be more adhesive towards the substrate due to the process of graphitization where carbon is precipitated from bulk nickel substrate [32]. It has also been proven that epitaxial formation of ‘fcc’ nickel provides the one of the strongest and stable adsorption site for carbon, thus ensuring proper synthesis of graphene [18].

2.7.4 SEM Imaging of Nickel

Electroless nickel deposition usually consist of pure nickel with slight variations in the composition of Ni_3P or Ni_3B. Often than not, electroless nickel deposition do not allow the formation of intermetallic compounds. This is because high number of atom movements through surface diffusion is needed for the growth of these tiny intermetallic compounds, especially to achieve the right stoichiometry of triple nickel atoms to one phosphorus, P or boron, B. Since the atom movement cannot occur before the deposition of the next layer of nickel atoms, these phosphorous and boron atoms get trapped between nickel atoms, which allows for a supersaturated nickel coating. The crystal structure of the electroless nickel depositions area of 'fcc'. A 'fcc' nickel has twelve atoms as its near neighbours, and for every twelve atoms, a grain is formed. Electroless nickel deposition has a microcrystalline size of 2 to 6 nm [35].

From the study made by [19], the optimal parameters for the sputtering process of nickel is by having a substrate-bias voltage of -90V, a working temperature of 770K, sputtering working power of 300W, and with an argon gas flow pressure of 5 mTorr. The reasons for these deposition parameters are to ensure growth of nickel films that are smooth as well as oriented in the ‹111› plane which is necessary for the growth of graphene [18]. A substrate bias -90V promotes nickel film growth that is rougher but with improved crystallinity, as well as allowing for a distinct ‹111› orientation. The roughness problem due to in bias voltage can be counteracted by increasing the deposition temperature to 770K. High temperatures allow for better atomic mobility which reduces amount of crack like microstructures as well as promotes more columnar structures that is relatively densely packed with grains. Figure A1 shows the formation of an increase in grain size when substrate temperature is increased from 570K to 770K. The reported that Argon pressure between 5 mTorr and 17.5 mTorr allows for a smoother nickel deposition where a lower pressure results in the smoothest nickel deposition as depicted in Figure A2. A deposition power of 300 W increases the probability of forming ‹111› crystal phases due to it requiring lower surface energy. Furthermore, relatively high deposition power reduces the formation of cracks as well as abnormal grain boundary growth (Figure A3) [19].

2.7.5 SEM Imaging of Graphene

Scanning Electron Microscopy (SEM) of graphene has been poorly documented as most researches have been focused towards the use of Transmission Electron Microscopy (TEM) as the produced graphene are of very thin layers. Experiment conducted by [36] managed to observe images of graphene on SiO_2 surface by collecting secondary electron that has been accelerated to 10 keV of energy. It was proven that the best range of primary electron acceleration voltage is between 0.5 to 1.5 kV (1.0 kV being optimal) as each individual graphene layer were able to be clearly distinguished, and is stated to be independent of the type of substrate used. This independence was proven by observing layers of graphene on other substrates such as mica and sapphire. Figure A4 shows the graphene layer observed using SEM at various primary electron acceleration voltage.

2.7.6 SEM Imaging of Steel-Nickel Interface

Intermetallic compounds formation occurs during the deposition of nickel on substrate. During the intermetallic compound formation, intermediate processes promote the precipitation of atoms from the said substrate into the deposited nickel. This intermediate process also known as age hardening, hardens the interface due straining effects caused by the difference in the interatomic spacing. In the case of steel and nickel inter-diffusion, a visible intermetallic phase (Figure A5) that improved the adhesion was formed [35].

2.7.7 SEM Imaging of Graphene-Nickel Interface

By exposing nickel during the pyrolysis of hydrocarbon, formation of different carbon containing surface phases are of high possibility. One of the common carbon containing surface phase is nickel carbide (Ni_2C). These Ni_2C phases are lattice matched with respect to ‹111› orientated nickel. During graphene growth at 500°C, these surface carbides are transformed into graphene [18]. This is supported by [37] where initial samples exhibited certain amount of surface carbides but soon disappeared as the temperature was increased. At graphene growth at a range of 500°C to 650°C, graphene grows directly on nickel substrate without any coexisting carbide

phases [18] [37]. At higher temperatures, such as 800 to 900C, higher concentration of carbon content is needed where graphene is grown through the precipitation of carbon (during cooling) after bulk diffusion (at elevated temperatures). During the cooling of nickel from these elevated temperatures (800°C and above), precipitations of carbon may result in carbide or second layer of graphene growth. In the research conducted by [37], it was also proved that carbide layers acts as an inhibitor for proper nucleation of graphene, thus reduction in surface carbide would promote proper graphene growth.

2.8 Research Gap

From the literature review that has been done, several research gaps have been identified. For the friction stir welding tool, the current tool improvement progress has been stagnant after the introduction of polycrystalline cubic boron nitride (PCBN). With the latest discovery of graphene as one of the strongest substance, this project intends to make use of that property to enhance the friction stir welding tool. Such enhancement of the tool has yet to be made thus proving the novelty of this project. In addition of that, very few study on chemical vapour deposition of nickel on steel substrate have been carried out therefore only minimal data, and information is available on the subject. This project intends to fill in the research gap by characterizing and analysing the methane based graphene synthesis on H13 tool steel though chemical vapour deposition.

.

CHAPTER 3
METHODOLOGY

3.1 Friction Stir Welding Tool

A friction stir welding (FSW) tool is to be manufactured using H13 steel rod with a CNC lathe machine. Appropriate design parameters such as speed of tool rotation (rpm) as well as the traverse speed (ms^{-1}) will be taken into consideration. This is because the penetration depth of the tool's pin correlates to the quality of the solid-state joint. Hence, the deeper the penetration of the pin, the greater the volume of material to be stirred, thus a better weld outcome [1] [4].

The shoulder of the FSW tool is a critical aspect as it has to be designed to produce and withstand high amount of heat due to the friction between the surface of the workpiece. The diameter of the shoulder should be of main focus as it effects the amount of frictional heat that could be generated. Studies have proven that an increase in tool diameter allow for higher frictional heat generation. However, it should be noted that a larger shoulder diameter causes an increase in the force on the workpiece which then affect the weld shape and mechanical properties. The shape of the shoulder should be taken into consideration as well. The main types of shoulder designs are flat, concave and convex shoulders [1] [2].

Aside the tool shoulder, the tool pin is equally important as assist in producing the necessary deformation and frictional heating in the workpiece. The main function of the pin is to provide adequate disruption of the workpiece by shearing the material in front of the tool's pin, and moving it to the rear of the pin. Furthermore, proper pin design has to be taken into consideration as it governs the depth of deformation as well as the tool travel speed. Some of the more common type of pin design include round-bottom cylindrical pin, flat-bottom cylindrical pin, and truncated cone pin [5].

A simple FSW tool is proposed via a sketch (Figure A6) in order to reduce the number of variable due to complex tool geometry. A simple tool allows for better understanding of the tool material without any major influencing factors that could arise from a complicated tool. Therefore, a tool with a flat shoulder end surface accompanied by a tapered conical pin was opted. The dimensions of this tool is as shown in Figure 3.1. Note that the corners of the tools are filleted to promote perfect graphene growth.

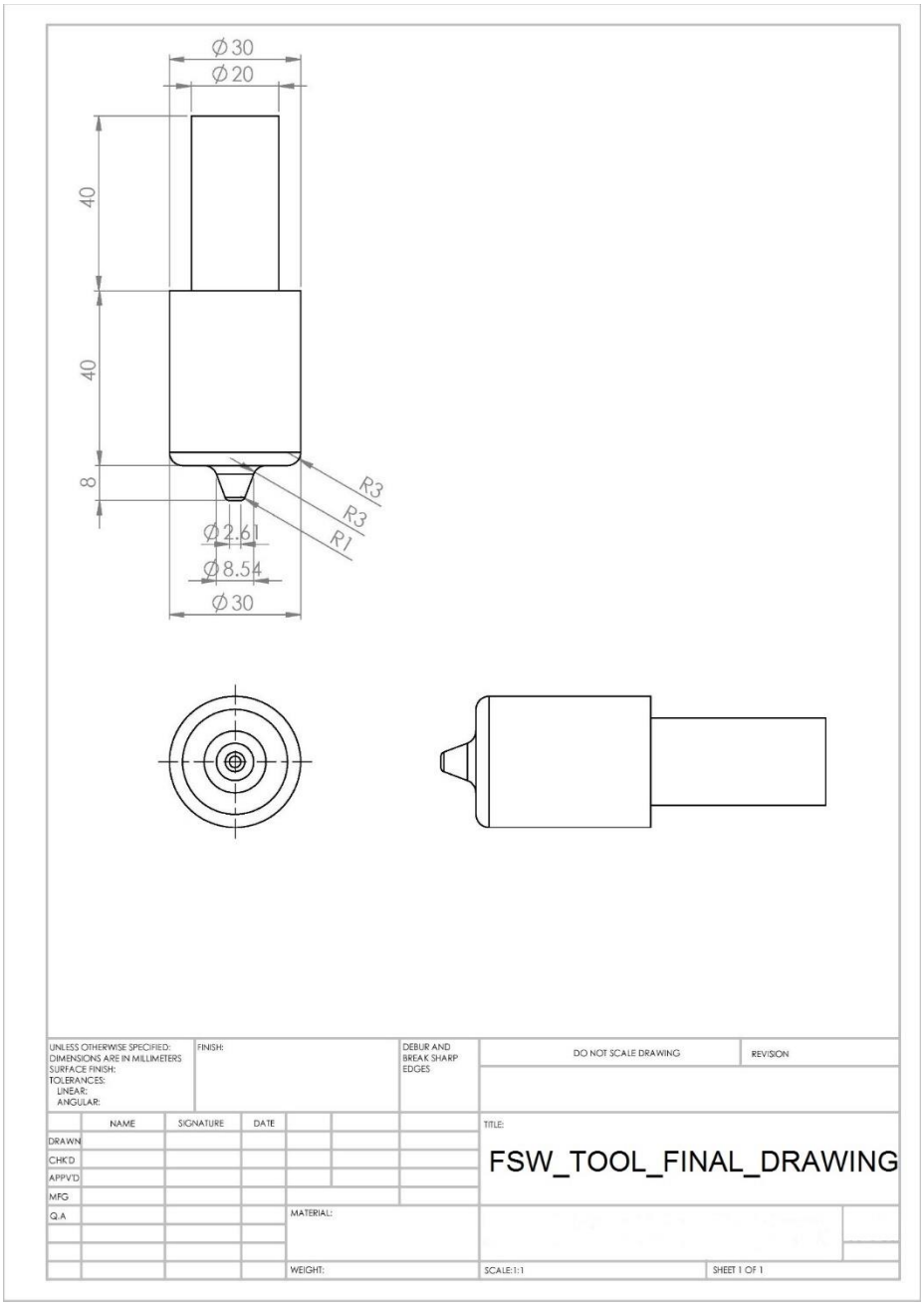

Figure 3.1: Dimensions of a simple FSW tool.

3.2 Heat Treatment of Friction Stir Welding Tool

The first step of heat treatment of H13 tool steel is the preheating cycle. Preheating cycle allows the molecules of the steel to be in a relaxed state so that molecule transformation could be applied. Since this FSW tool is quite large and is of intricate design, the recommended preheating temperature is 650°C, held for 15 minutes. After the preheating cycle, the furnace should be raised to a temperature of 1010°C to facilitate the soaking cycle. The temperature is set as such because of the it is the austenizing temperature of H13 tool steel. The soaking time of 17 minutes is stipulated due to the smallest cross-section (tool pin) being 8mm thick [38].

After the soaking cycle, the tool is to be removed from the furnace and placed on a cooling rack that is set in room temperature to facilitate the quenching cycle. After removal of the tool, the furnace is cooled to a temperature of 65°C, similarly to the FSW tool. The final step, which is the tempering cycle is the utmost critical process. Once the FSW tool reaches a temperature of 65°C, the tool is loaded into the furnace, and the temperature of the furnace is raised to 565°C. Once, the furnace has reach a temperature of 565°C, the tool is allowed to temper for a minimum of 2 hours. This is so that slow heat transferring process could take place, as well as allowing transformation of austenite into stable martensite (reduced brittleness). After 2 hours of the tempering cycle, the tool is removed from the furnace to be cooled to room temperature. This entire cycle of heat treatment of H13 tool is illustrated by Figure 3.2 [38].

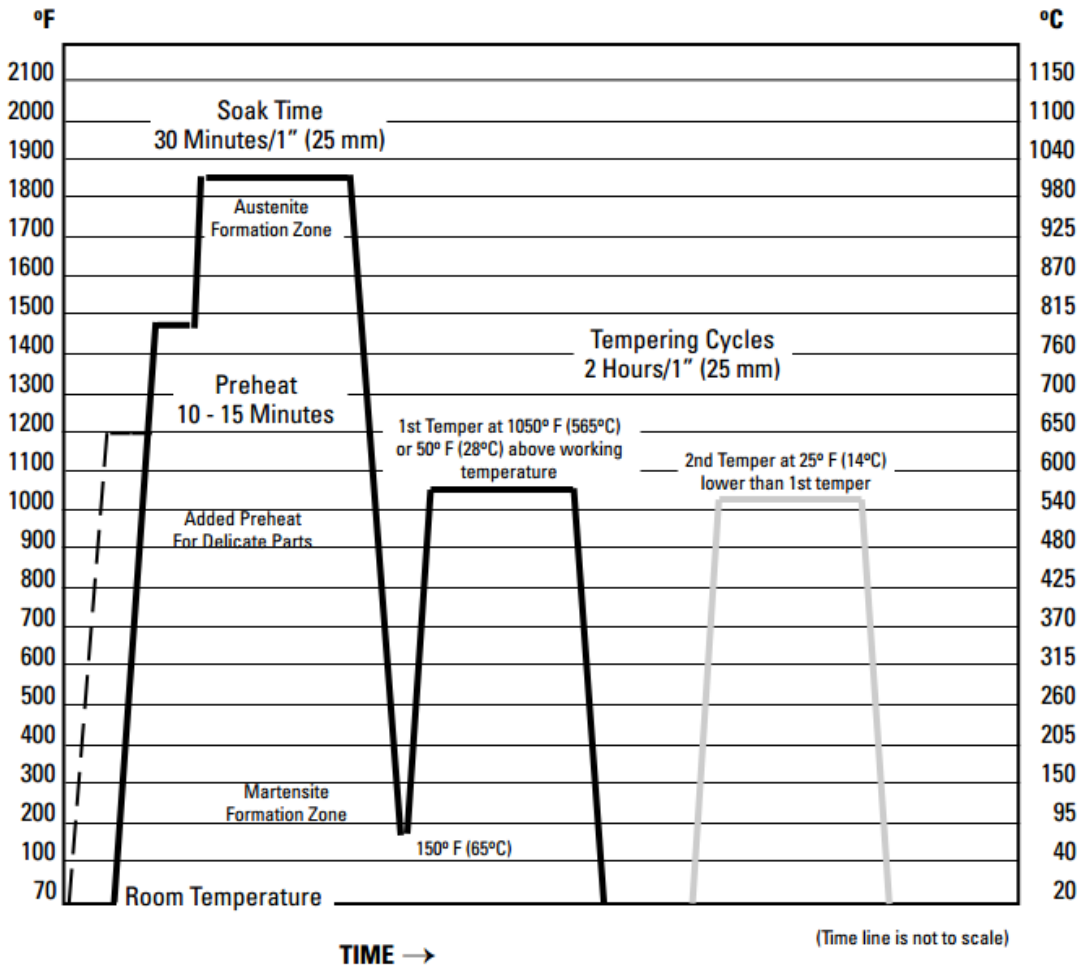

Figure 3.2: Graph representing the temperature and heating period for proper heat treatment of H13 tool steel [38].

3.3 Magnetron Sputtering for Nickel Deposition

A Magnetron Sputtering machine is to be used to deposit approximately 5µm thick nickel coating onto H13 tool steel friction stir welding tool. The Magnetron Sputtering machine has a vacuum chamber for the purpose of the actual plasma vapour deposition process. A vacuum pump is used to ensure and control the vacuum pressure of the vacuum chamber. The Mass Flow Controllers are used to control and maintain the required gas volumes needed for the plasma generation. Finally, after the deposition process, the exhaust lines are used to discharge exhaust gases from the vacuum chamber [39].

Plasma vapour deposition, also known as sputtering process is recommended to be conducted in a vacuum level of less than 5 x 10^{-5} Torr. Pre-sputtering process can be

conducted to remove oxidation layers from workpiece surface. For the pre-sputtering, the throttle valve position of the Magnetron Sputtering machine has to be set between 20% to 40% with Argon gas flow at 50 to 100 sccm, while the working pressure would be between 2 to 5 x 10^{-5} Torr. DC power or RF power with run-time should be set for the deposition layer. A higher power, and longer run time corresponds to a higher deposition rate, and thicker deposition film. After the process of deposition, the vacuum pressure is set to a lower value while keeping the plasma sustained [39]. Table 3.1 below shows the parameter used for the sputtering process using the Magnetron Sputtering machine based on [19] study.

Table 3.1: Parameters that were used for the nickel sputtering process.

Parameters	**Values**
Working Power	100 Watts
Argon Pressure	9.6 mTorr
Argon Flow Rate	80 sccm
Substrate Temperature	500°C
Sputtering Duration	300 seconds

3.4 Chemical Vapour Deposition for Graphene Synthesis

Chemical vapour deposition (CVD) will be used to apply a layer of graphene atop of nickel coated H13 steel tool. The main components of a CVD process are the gas delivery system, a reactor, and a gas removal system as illustrated in Figure 3.3. Despite a simple setup, CVD process require proper parameter controls to ensure proper layer formation. Some of the basic parameters include the operating pressure, temperature, duration, boundary layer profile over the substrate, pyrolysis of precursor, rate of reaction, grain boundary or defects of substrate, and the presence of catalyst [21]. Before proceeding with any CVD process, the substrate will be subjected to dry nitrogen blowing to ensure the its surface is clear from solvent dirt and residue [32].

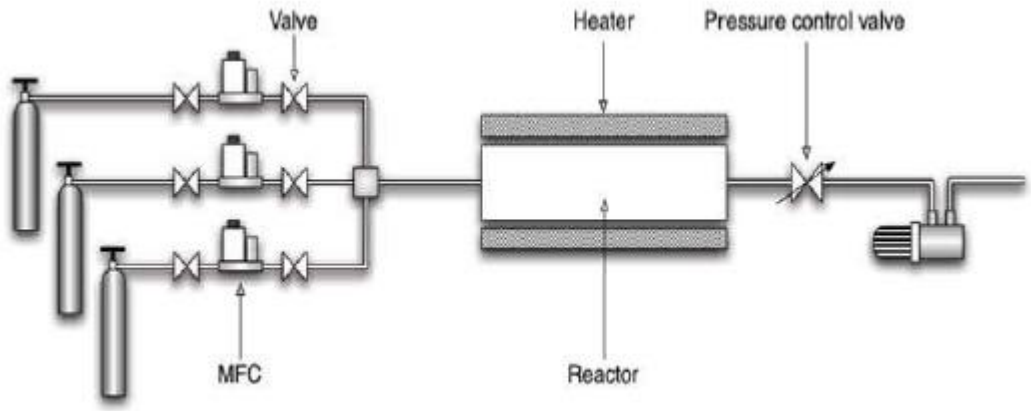

Figure 3.3: Schematic diagram of a CVD process setup. The MFC controls the gas delivery into the reactor while the chemical vapour deposition of the precursor takes place in the reactor. After a certain duration, vacuums are used to remove the precursor by-products [21].

Nickel coated H13 tool steel substrate will be placed in an ambient pressure thermal chemical vapour deposition reactor. The reactor is cleaned by purging H_2 gas for approximately 5 minutes. The temperature of the reactor is raised to 1000°C while being introduced with H_2 at a rate of 200 sccm and Argon at a rate of 500 sccm. The process of raising the temperature to 100°C takes approximately 45 minutes with the aforementioned H_2 and Argon gas acting as the carrier gas. After reaching the desired temperature, the selected precursor gas, methane would be flowed to the reactor for a duration of 20 minutes at a rate of 60 sccm. Pyrolysis of precursor gas, methane would allow for the deposition of graphene layer on nickel substrate. After 20 minutes of graphene deposition, the deposition chamber is allowed to cool at a steady state which takes approximately 1 hour. The graphene deposition substrate is removed when the temperature of the reactor reaches approximately 25°C [40].

3.5 Raman Spectroscopy

Raman spectroscopy will be conducted with a spectral resolution of 4 cm^{-1}, and using an argon ion laser that has a wavelength of 514.5 nm. Data collection of the Raman spectra was done with the use of a high throughput holographic imaging spectrograph. In addition to that, Raman spectra was conducted at standard room temperature and pressure. Based on the Raman spectrum obtained by Raman spectroscopy, three prominent peaks could determine the presence of graphene, as depicted in Figure 3.5.

These peaks are the D-line which is located at 1350 1/cm, the G-line which is located at 1580 1/cm, and the 2D-line which is located approximately at 2675 1/cm. The peak that occur at the D-line can be used to determine the amount of defect that is present in the synthesized graphene. It should be noted that the presence of the D-line could be due to the presence of grain boundaries, or chemical doping after effects [41].

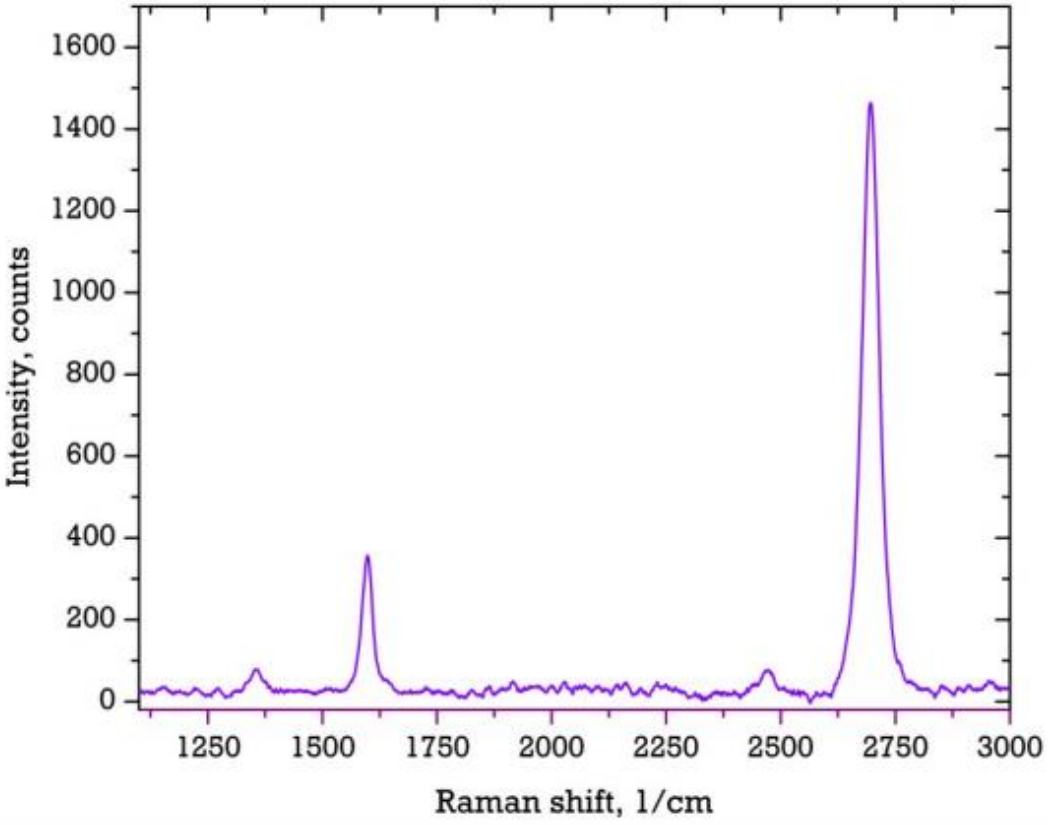

Figure 3.4: Raman spectrum of a monolayer graphene with prominent peaks. [41]

3.6 X-Ray Photoelectron Spectroscopy (XPS)

X-Ray photoelectron spectroscopy (XPS) is a method used to characterize the surface composition of a material. For graphene study, XPS is used to determine the presence of graphene by exciting the electrons and capturing photoelectrons from specific shells, in this case C1s. Photoelectrons from C1s usually has a binding energy of 286 ± 1 eV which is a feature of double-bonded carbon sp^2 bonds [23] [29] [30].

3.7 Scanning Electron Microscopy (SEM)

An electron microscope equipped with an Energy Dispersive Spectro (EDS) is to be used to determine any abnormalities or surface defects (i.e. cracks) that would be present at the material interface. The two main interface in concern are the nickel-steel interface, and the graphene-nickel interface. Images of the interface would be recorded at several magnifications (minimum of 100x).

3.8 Energy Dispersive Spectroscopy (EDS)

Energy Dispersive Spectroscopy (EDS) is to be used to determine the type of element present along the cross section of the nickel and graphene coated friction stir welding tool. The percentage of elements will be recorded and tabulated.

3.9 Proposed Gantt Chart

Table 3.1: Proposed Gantt chart measured in weeks.

Content	Allocation/ Week	1	2	3	4	5	6	7	8	9	10	11	12	13	14
Project title selection: Study on graphene-nickel interface on steel in friction stir welding (FSW) tool	1 day														
Consulation with Supervisor	Every week														
Topic Introduction (FYP 1)															
Background study Problem Statement Objective Scope of Study	1 week														
Review of Problem Statement & Objective Confirmation of Problem Statement & Objective	1 week														
Literature Review (FYP 1)															
Current FSW tool Properties of graphene Advantages of nickel coating Nickel coating on steel via chemical vapour deposition (CVD) Graphene application via CVD Properties of CVD grown graphene	2 weeks														
Review of literature review Confirmation of literature review	1 week						▲								
Design & Test Methodology (FYP 1)															
FSW tool design CVD process Raman Spectra, XPS, FE-SEM with EDS, TEM	2 weeks														
Review methodology Confirmation of methodology	2 week														
Review design parameters Confirmation of design parameters	3 weeks														

Table 3.1: Proposed Gantt chart measured in weeks. (Continuation)

Content	Allocation/ Week	1	2	3	4	5	6	7	8	9	10	11	12	13	14
Design & Test Preparation (FYP 1)															
Preparation of FSW tool material Prepation of CVD Chemicals Confirmation of lab equipment availability	2 weeks														
Actual Design & Test (FYP 1)															
Fabrication of FSW tool	2 weeks														▲
Content	**Allocation/ Week**	**15 (1)**	**16 (2)**	**17 (3)**	**18 (4)**	**19 (5)**	**20 (6)**	**21 (7)**	**22 (8)**	**23 (9)**	**24 (10)**	**25 (11)**	**26 (12)**	**27 (13)**	**28 (14)**
Consulation with Supervisor	Every week														
Actual Design & Test (FYP 2)															
Magnetron Sputtering of Nickel on Steel	1 week														
CVD Process of Graphene on Nickel	1 week														
Raman Spectra	1 day														
XPS	1 day														
FE-SEM with EDS	1 week														
TEM	1 day														
Test completion & result verification	1 week										▲				
Results & Discussion (FYP 2)															
Data tabulation	5 weeks														
Analysis on Raman Spectra, XPS, FE-SEM with EDS, TEM	5 weeks														
Results comparison & validation Project discussion	3 weeks														
Review results & discussion Confirmation of results & discussion	1 week										▲				
Recommendation & Conclusion (FYP 2)															
Design recommendation Test recommendation	1 week														
Conclusion	1 week														
Review recommendation & conclusion Confirmation of recommend. & concl.	1 week											▲			

3.10 Key Milestones

Table 3.2: Key milestones of project.

FYP 1	
Week	**Content/Activity**
6	Review and confirmation of literature review
14	Fabrication of FSW tool
FYP 2	
Week	**Content Activity**
24	Raman Spectra, XPS and FE-SEM & EDS completion
24	Review and confirmation of project results & discussion
25	Review and confirmation of recommendation & conclusion

3.11 Project Flow Chart

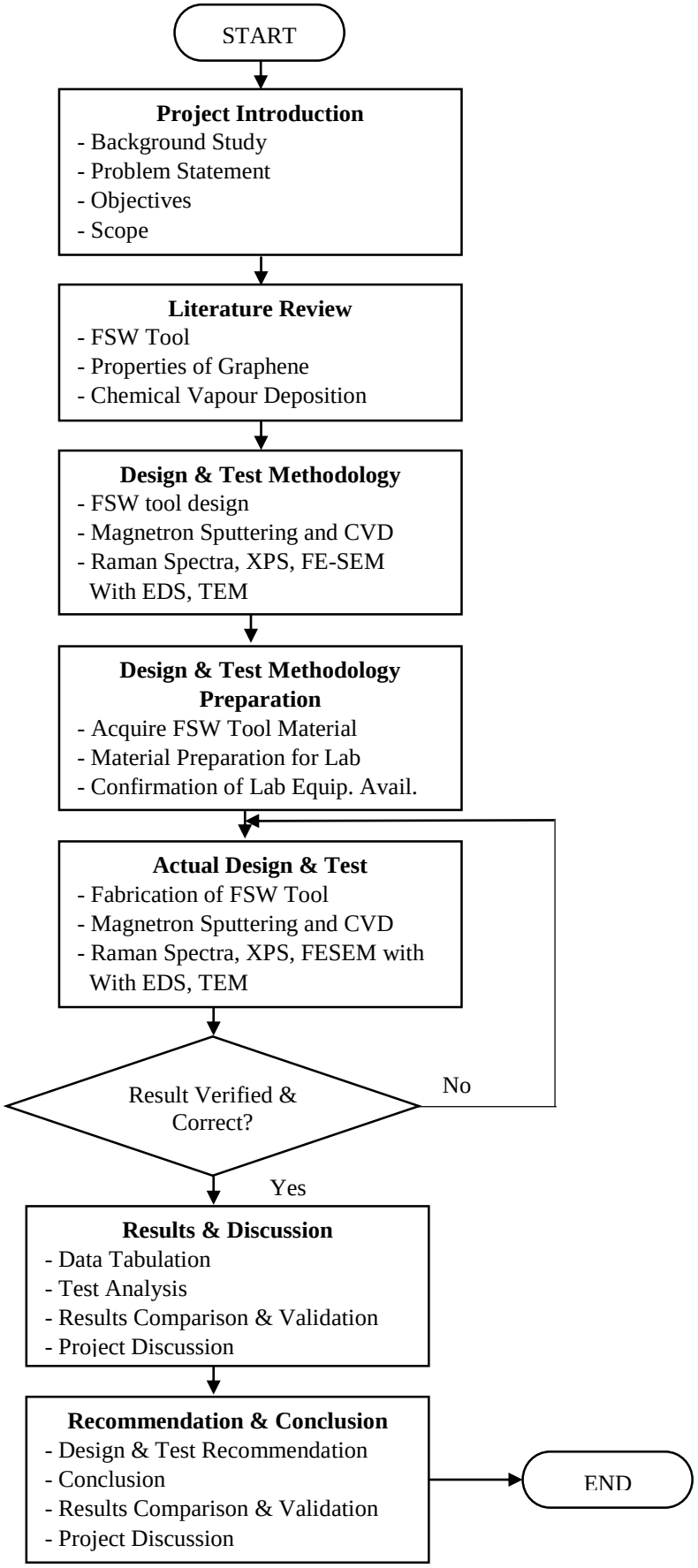

Figure 3.5: Project flow chart

CHAPTER 4
RESULTS AND DISCUSSION

4.1 Raman Spectroscopy

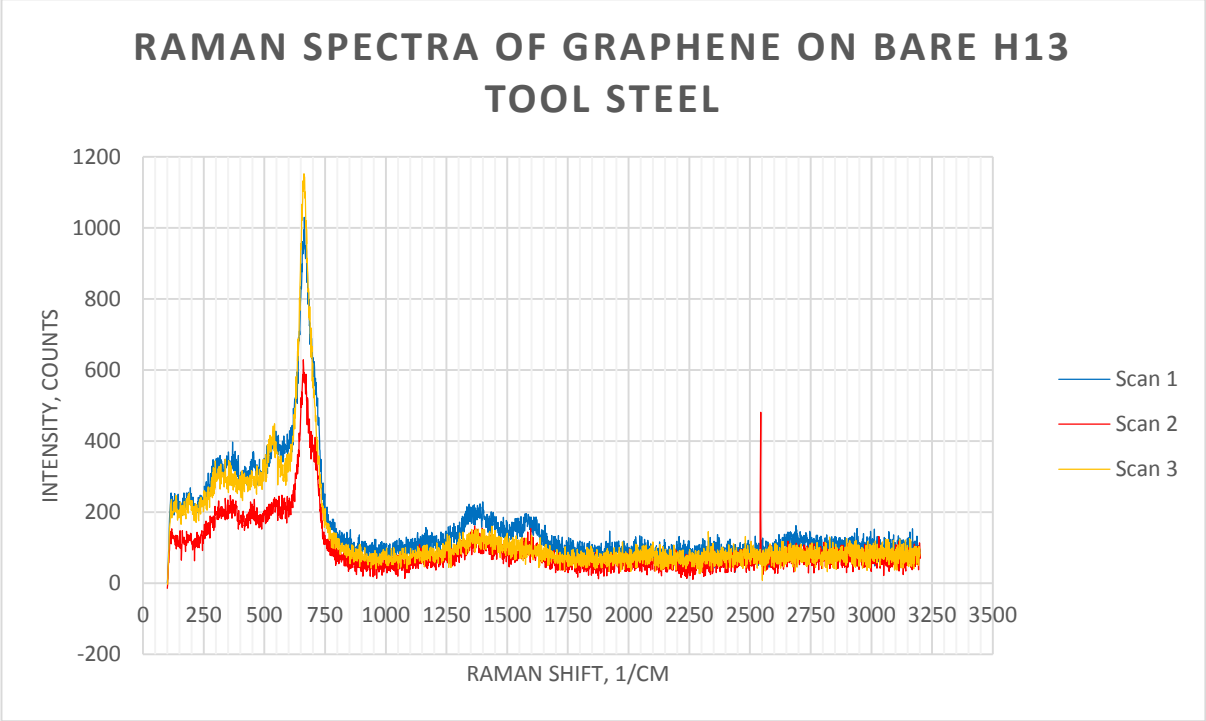

Figure 4.1: Raman spectra of graphene on bare H13 tool steel.

Table 4.1: Tabulated data for Raman spectra of graphene on bare H13 tool steel.

Raman Spectra	Major Peak		D Peak		G Peak		2D Peak		Ratio
	Loc. (counts)	*Inten. (cm^{-1})*	*Loc. (counts)*	*Inten. (cm^{-1})*	*Loc. (counts)*	*Inten. (cm^{-1})*	*Loc. (counts)*	*Inten. (cm^{-1})*	I_G/I_{2D}
Scan 1	664.81	1029.58	1399.85	229.2	1579.76	195.91	2689.96	162.24	1.2
Scan 2	629.05	660.18	1366.26	161.605	1596.08	154.638	2544.15	481.14	0.3
Scan 3	662.50	1152.5	1437.45	160.816	1500.71	140.46	2504.27	118.12	1.2

The characteristics of graphene based on Raman are two peaks which are the G and 2D peaks. The G peak occurs at a Raman shift of ~1580cm^{-1} which is due to the in-

plane vibration of sp2 carbon atoms, while the 2D peak occurs at a Raman shift of ~2675cm^{-1} which is due to the stacking order of graphene sheets. Figure 4.1 indicates the Raman spectra of graphene at the 3 different location which are indicated by 3 different scan lines plots. Table 4.1 is a tabulation of the major peaks for respective Raman spectra line scans. Aside from the characteristic Raman spectra peaks of graphene, the results indicate a relatively high intensity peak at ~662cm^{-1}. This particular high intensity peak does not belong to graphene, but may be due to constituents of the H13 tool steel which are Chromium, Molybdenum, Silicon, and Vanadium as reported by [23].

The Raman spectra revealed D peaks which are present in cases where there are defects in the synthesized graphene. The defects may be due to surface dislocations, corrugation, interaction of graphene with substrate, as well due to accidental doping [22]. The low intensity of D peak is characteristic of low defect graphene, as well as graphite. In these results, it is possible that the D peak points towards the formation of graphite due to it not being a sharp peak but a broad peak with a higher FWHM [22]. Low intensity of the G and 2D peaks suggests the possibility of the H13 tool steel substrate has undergone carburization or developed a layer very thin layer of graphite instead of graphene [28]. However, it should be noted that Raman spectra intensity of below 1000 counts has been reported for graphene coated on bare stainless steel [24]. In addition to that, the multiple layers of graphene and graphite have been proven to show low 2D intensity as well as low peak symmetry. This is based on the linear progression where the increase in number of carbon layers corresponds to a decrease in Raman spectra intensity [26] [27].

An analysis was done on the G and 2D ratio, I_G/I_{2D} for all 3 locations. Location 1 and 3 show a good co-relation to multi-layer graphene growth. This is because multi-layer graphene characteristically has a 2D peak that is about 2 to 4 times lower than the G peak which allows for an I_G/I_{2D} ratio of greater than 0.25 [27]. Even though the I_G/I_{2D} ratio seem to be fitting for multi-layer graphene, a contradicting factor in regard to the intensity of the comes into view. This is because, it is typical for multi-layer graphene to have a higher intensity due to higher detection of carbon concentration [22] [29]. It has also been reported that multi-layer graphene has a much asymmetrical, and broader 2D peak, instead of a symmetrical and sharp 2D peak which is usually detected for

single layer graphene [22] [26]. For this case, location 1 and location 3 show a broad peak which suggest for multi-layer graphene synthesis. On the other hand, location 2 has an I_G/I_{2D} ratio of 0.3 with a relatively weaker G band. This may suggest the formation of single layer graphene as the 2D peak is usually 2 to 4 times higher than the G peak [24] [26] [27]. This is in line with a report where single layer graphene deposition without nickel catalyst on stainless steel revealed an I_G/I_{2D} ratio of 0.4 to 1.0 [24] [25]. This theory has to be tested via visual examinations as report by [24] showed that characteristic graphene peaks were present for allegedly graphene coated stainless steel but graphene was absent during visual inspection.

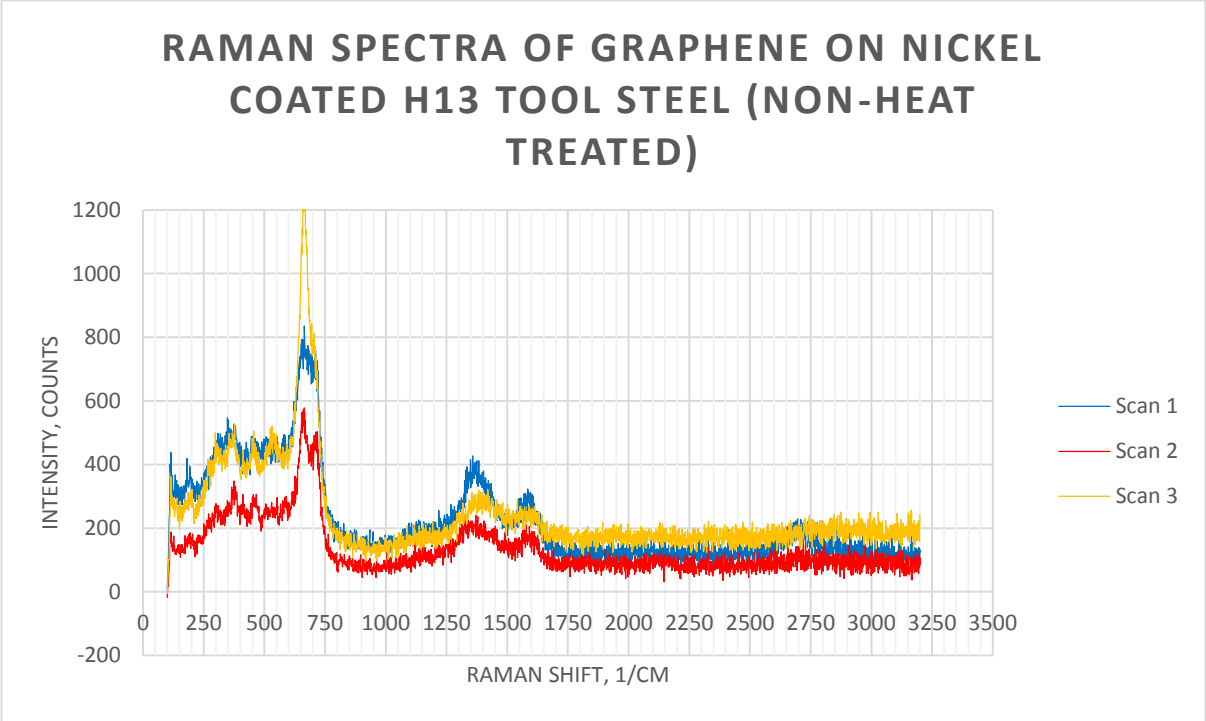

Figure 4.2: Raman spectra of graphene on nickel coated H13 tool steel.

Table 4.2: Tabulated data for Raman spectra of graphene on nickel coated H13 tool steel.

Raman Spectra	**Major Peak**		**D Peak**		**G Peak**		**2D Peak**		**Ratio**
	Loc. (counts)	***Inten. (cm^{-1})***	***Loc. (counts)***	***Inten. (cm^{-1})***	***Loc. (counts)***	***Inten. (cm^{-1})***	***Loc. (counts)***	***Inten. (cm^{-1})***	***I_G/I_{2D}***
Scan 1	664.81	834.91	1357.84	427.277	1584.86	323.49	2696	229.103	1.4
Scan 2	663.65	577.43	1370.47	240.171	1577.72	210.543	2728.67	154.52	1.36
Scan 3	662.50	1245.5	1419.72	320.836	1541.88	289.86	2744.95	239.70	1.21

Figure 4.2 indicates the Raman spectra of graphene on nickel coated H13 tool steel at the 3 different location which are indicated by 3 different scan lines plots. Table 4.2 is a tabulation of the major peaks for respective Raman spectra line scans. Similar to the Raman spectra for graphene on bare H13 tool steel (Figure 4.1), the Raman spectra for nickel coated H13 tool steel revealed a major peak with a relatively high intensity at Raman shift of ~663cm^{-1}. As explained earlier, this peak may be due to the constituent of H13 tool steel, as well as due to the nickel coating [23].

Even with the presence of Nickel coating as a catalyst (later proved to be non-existent through XPS and EDS), there were presence of D peaks in the Raman spectra on all locations which is similar to report by [24] [25]. It should be noted that typically the D peak should be present at ~1350cm-1, and even up to ~1370cm^{-1} for graphene coated on nickel [26] [27] [25]. Location 1 and 2 show a D peak at locations 1357.84cm^{-1} and 1370.47cm^{-1} which is consistent with current literatures. Location 3 however show a much higher location of D peak, at 1419.72cm^{-1} which could be a due to red-shifting of Raman spectra. The shifting of peak is often due to strain effects on the graphene by the substrate [22].

The G peak for location 1 and 2 is consistent with current literature which is 1580cm^{-1} and 1590cm^{-1} for graphene synthesis on silicon carbide sheet and nickel seed respectively [22] [25]. A blue-shifted G peak of approximately ~40cm^{-1} was found for location 3. A shift in G peak is common in silicon carbide substrates due to lattice mismatch, however the reason for the blue-shift is unknown for this particular substrate [22]. A 2D peak is vital for graphene determination as it is characteristic of graphene due to the involvement of phonons near the K point [26] [27]. A broad and extremely low intensity 2D peak was present for all three locations on this substrate which may suggests for a presence of multi-layer graphene [23] [22] [29]. This is supported by a high I_G/I_{2D} ratio for all three locations on this substrate. However, the presence of multi-layer graphene is questionable as the intensity of all the 2D peak are relatively similar to the background noise which is similar to discontinuous graphitic domain [28].

Focusing towards the intensity, low Raman spectra intensity has been reported for nickel-iron (NiFe) alloy as depicted in Figure 4.3 [22].This reported Raman spectra

intensity is consistent with the Raman spectra intensity obtained for all locations of this nickel coated H13 tool steel substrate. This however does not explain for the extremely low intensity of 2D peaks.

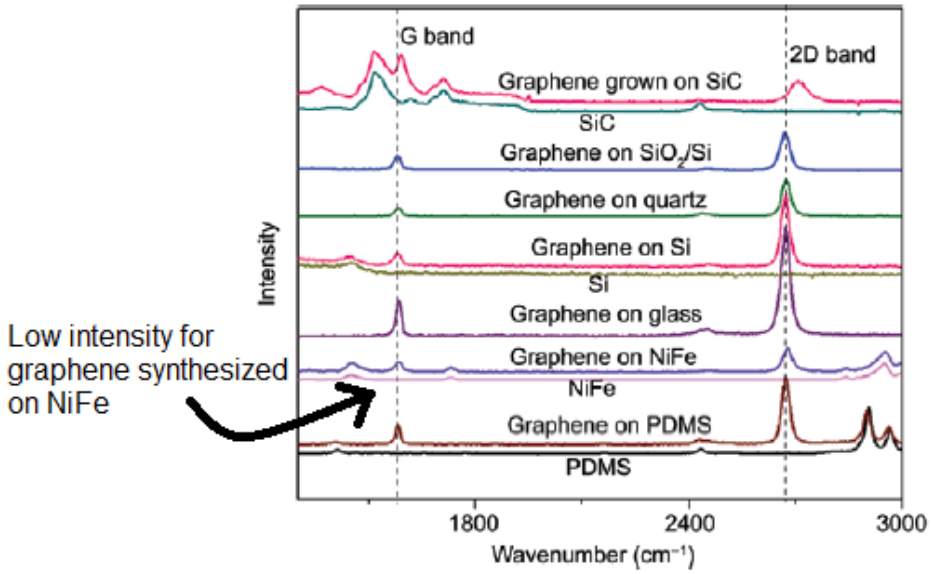

Figure 4.3: Illustration of the Raman spectra intensity for multiple substrate [22].

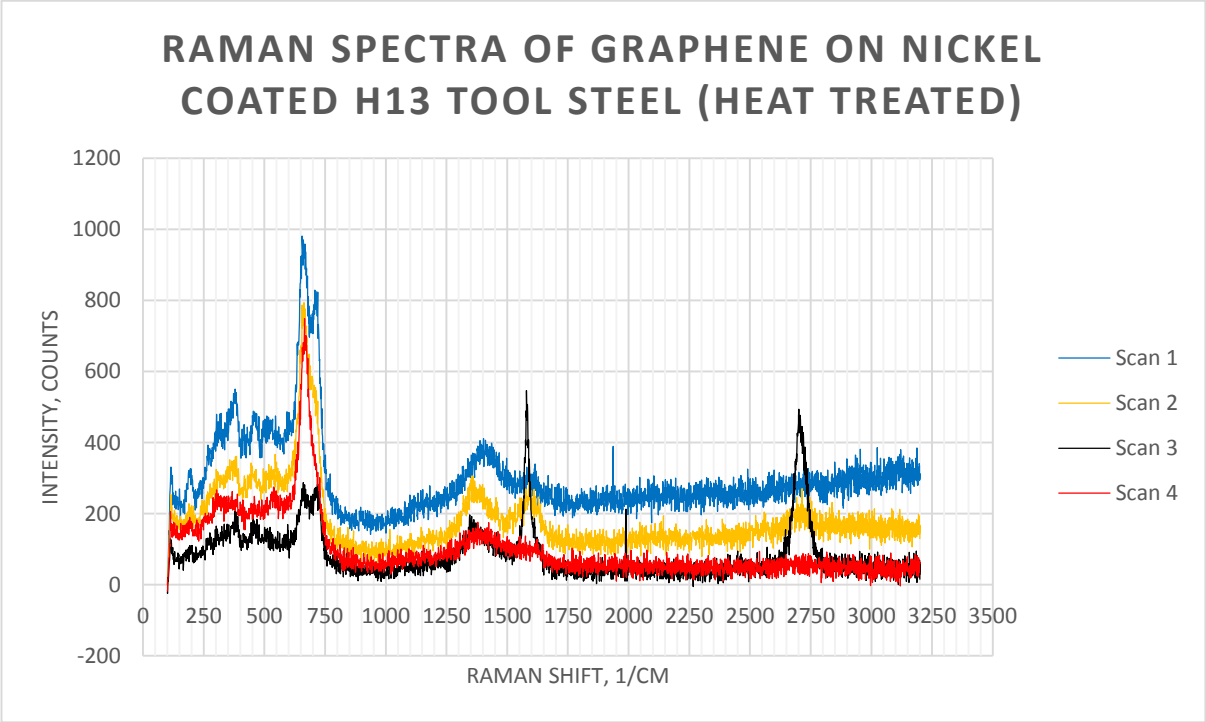

Figure 4.4: Raman spectra of graphene on nickel coated heat treated H13 tool steel.

Table 4.3: Tabulated data for Raman spectra of graphene on nickel coated heat treated H13 tool steel.

Raman Spectra	Major Peak		D Peak		G Peak		2D Peak		Ratio
	Loc. (counts)	***Inten. (cm^{-1})***	***Loc. (counts)***	***Inten. (cm^{-1})***	***Loc. (counts)***	***Inten. (cm^{-1})***	***Loc. (counts)***	***Inten. (cm^{-1})***	I_G/I_{2D}
Scan 1	655.56	980.816	1401.94	410.8	1615.4	339.665	2738.96	327.08	1.04
Scan 2	662.50	793.58	1355.74	306.13	1589.96	291.84	2714.08	270.50	1.08
Scan 3	660.18	287.50	1346.25	196.71	1579.76	546.10	2701.17	493.42	1.11
Scan 4	665.96	748.50	1378.88	176.17	1574.65	137.04	2539.73	93.33	1.47

Figure 4.4 indicates the Raman spectra of graphene on nickel coat heat treated H13 tool steel at the 3 different location which are indicated by 3 different scan lines plots. Table 4.3 is a tabulation of the major peaks for respective Raman spectra line scans. The reason for this substrate is to determine whether heat treatment would affect the synthesis of graphene. Similar to the Raman spectra for graphene on bare H13 tool steel (Figure 4.1) and graphene on nickel coated H13 tool steel (Figure 4.2), the Raman spectra for nickel coated heat treated H13 tool steel revealed a major peak with a relatively high intensity at Raman shift of ~660cm^{-1} except for location 3. In addition to that, the peaks are not as symmetrical in comparison to the previous substrates. As explained earlier, this peak may be due to the constituent of H13 tool steel, as well as due to the nickel coating [23].

Similarly, nickel coated heat treated H13 tool steel revealed a D peak even with the presence of catalytic nickel coating. The D peak intensity for location 1 and 2 are similar to the D peaks obtained in the Raman spectra of nickel coated H13 tool steel which is between 240 and 430 counts. Location 3 and 4 however showed lower D peak intensity suggesting lower amount of defects of the synthesized graphene [24] [25]. Only location 2 show a D peak that is within the reported range of between 1350cm^{-1} and 1370cm^{-1}, while location 1 and 4 show red-shifted D peaks, and location 3 show a blue-shifted D peak [26] [27] [25].

The G peaks on this substrate were similar to that of nickel coated H13 tool steel except for Location 3. For location 3, G peak is located at 1579.76 which close to 1580cm^{-1} and 1582.5 cm^{-1} reported by literatures. In addition to that, the peak is prominent, sharp and relatively high intensity; showing a high in-plane vibration of sp^2 carbon atom [23]

[22]. Furthermore, this G peak location has been identified in Raman spectra of nickel-iron alloy [22]. However, the intensity of the G peak is not consistent with findings of [22] where the reported G peak is of low intensity (Figure 4.3) while the peak obtained for location 3 is relatively high. Similarly, the 2D peaks were similar to nickel coated H13 tool steel substrate, as location 1, 2 and 3 has blue-shifted 2D peaks while location 4 showed an absence of any peak. Focusing on intensity of the 2D peaks, only location 3 showed a relatively high intensity.

The G and 2D peaks were made into ratios, I_G/I_{2D} which is important in graphene thickness determination. For all locations, a I_G/I_{2D} ratio of greater than 1.0 was found which suggests the presence of multi-layer graphene based on reports by [23] [22] [29]. This is also supported by an asymmetrical, and broader 2D which is common for multi-layer graphene [22] [26]. In regard to intensity, all 4 locations show a very low intensity that suggest for presence of single layer graphene which contradicts with the presence of multi-layer graphene based on the I_G/I_{2D} ratio. Even though location 3 showed a relatively high intensity for the G and 2D peaks, report by [26] show that a minimum intensity of 1000 counts has to be reach to prove the presence of multi-layer graphene.

4.2 X-Ray Photoelectron Spectroscopy (XPS)

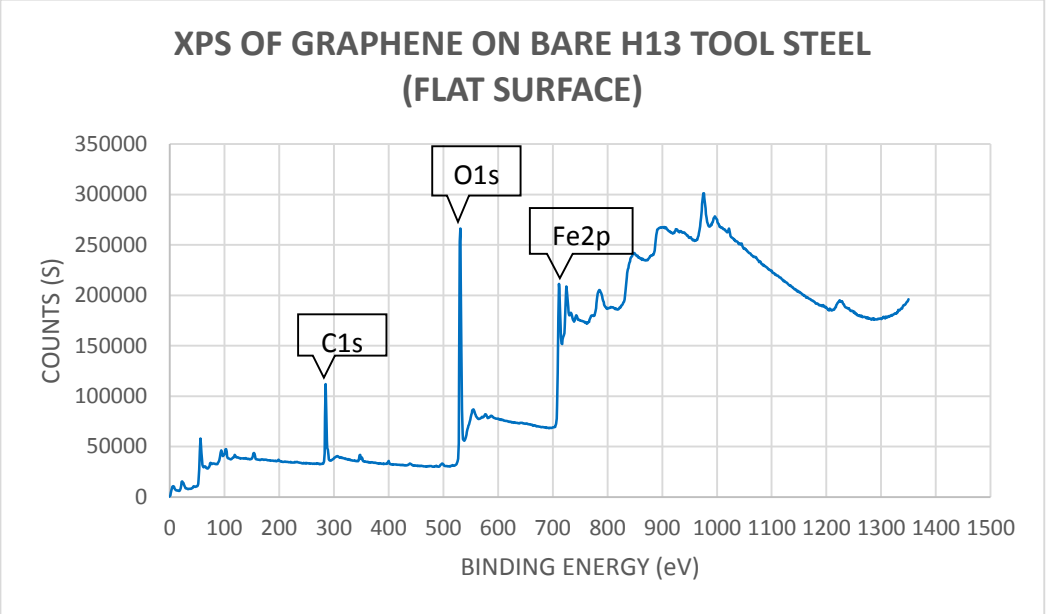

Figure 4.5: XPS of graphene on the flat surface of bare H13 tool steel.

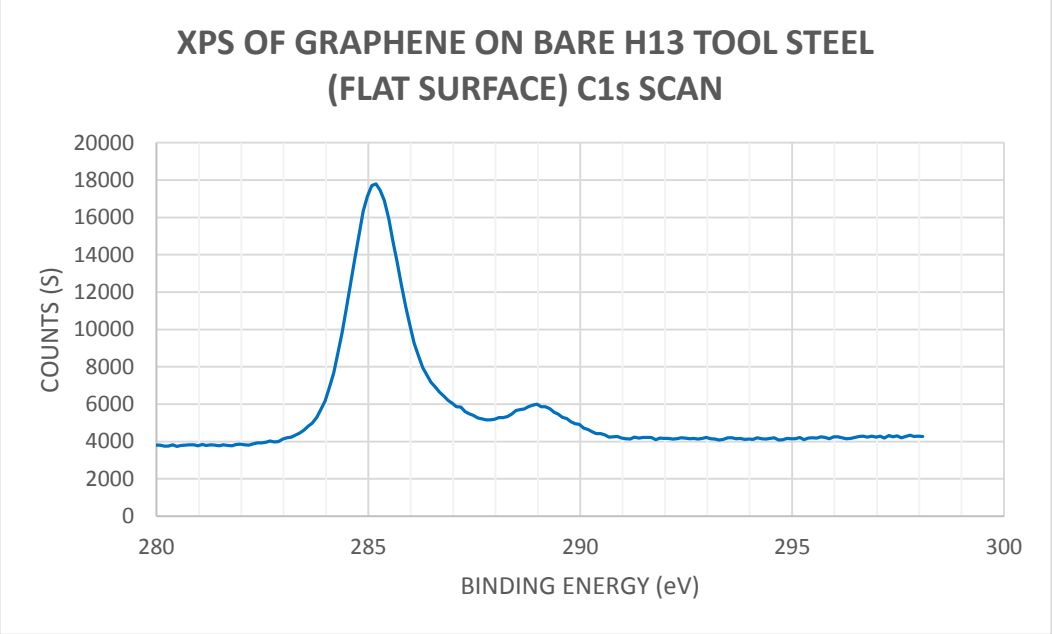

Figure 4.6: C1s XPS scan of graphene on the flat surface of bare H13 tool steel.

Table 4.4: Tabulated data for XPS of graphene on the flat surface of bare H13 tool steel.

Element (Shell)	Start BE	Peak BE	End BE	Height Counts	FWHM eV	Area (P) CPS.eV	Area (N)	At. %
O1s	538.08	530.99	523.08	220490	3.63	858531	4772	44.4
Fe2p	739.08	711.38	698.08	117640	4.72	1166046	1311.2	12.2
C1s	294.58	285.16	278.08	67828	2.86	236974	3364.1	31.3

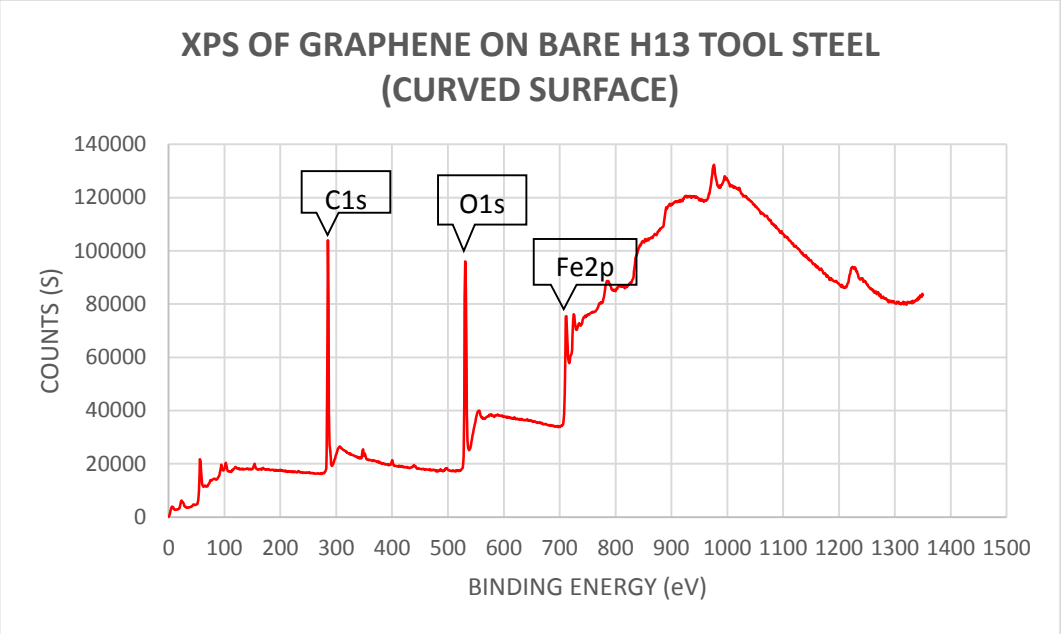

Figure 4.7: XPS of graphene on the curved surface of bare H13 tool steel.

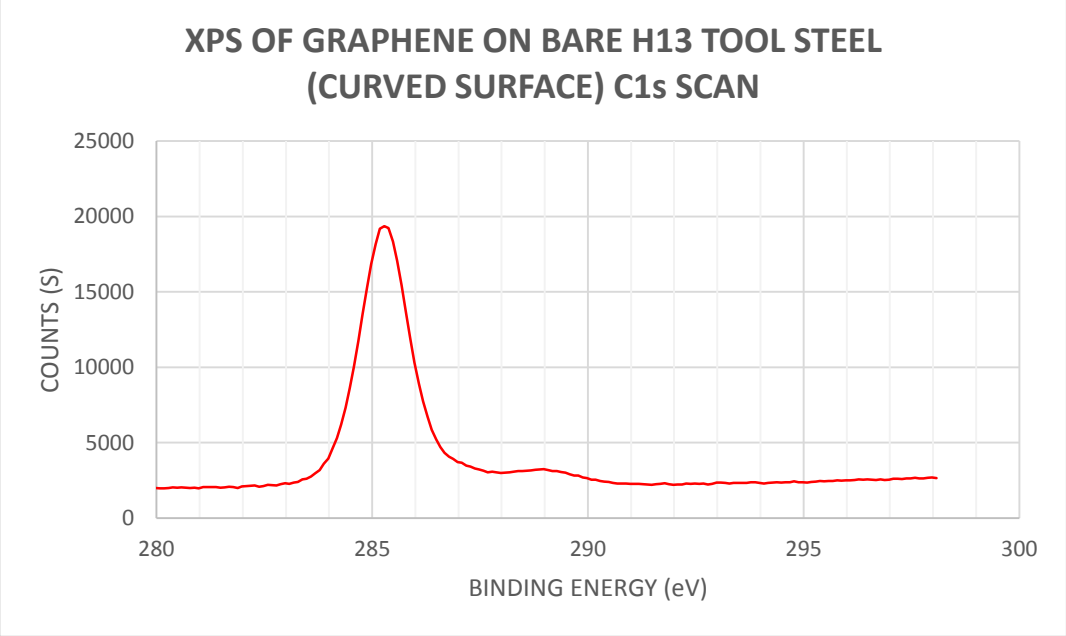

Figure 4.8: C1s XPS scan of graphene on the curved surface of bare H13 tool steel.

Table 4.5: Tabulated data for XPS of graphene on the curved surface of bare H13 tool steel.

Element (Shell)	Start BE	Peak BE	End BE	Height Counts	FWHM eV	Area (P) CPS.eV	Area (N)	At. %
O1s	538.08	531.2	523.08	73571	3.64	284253	1580.2	28.8
Fe2p	738.08	711.37	698.08	30504	4.1	212928	239.53	4.36
C1s	292.08	285.25	277.58	74448	2.64	236838	3362.3	61.28

Figure 4.5 illustrates the XPS survey spectra of graphene on bare H13 tool steel at the flat surface while Figure 4.7 illustrates the XPS survey spectra of graphene on bare H13 tool steel at the curved surface. From Figure 4.4 and 4.7, three prominent peaks are determined to be of O1s, C1s, and Fe2p. For graphene characterization, the presence of C1s peak is critical. Both flat and curved surfaces show C1s peak at a binding energy of 285.16 eV and 285.25 eV which is consistent with the reports made by [23] [30] [29] . It is important to note that C1s peak usually occurs at between 284 to 285 eV and relates to the covalent sp^2 hybridization of carbon, and the hexagonal lattice structure of carbon [23] [30] [29]. A detailed view of the C1s peak of both flat and curved surface are illustrated by Figure 4.6 and Figure 4.8 respectively. Based on the tabulated data in Table 4.4 and Table 4.5, for the flat surface, there has a lower C1s atomic percentage at 31.3%, in comparison the curved surface which has a C1s atomics percentage at 61.28 %.

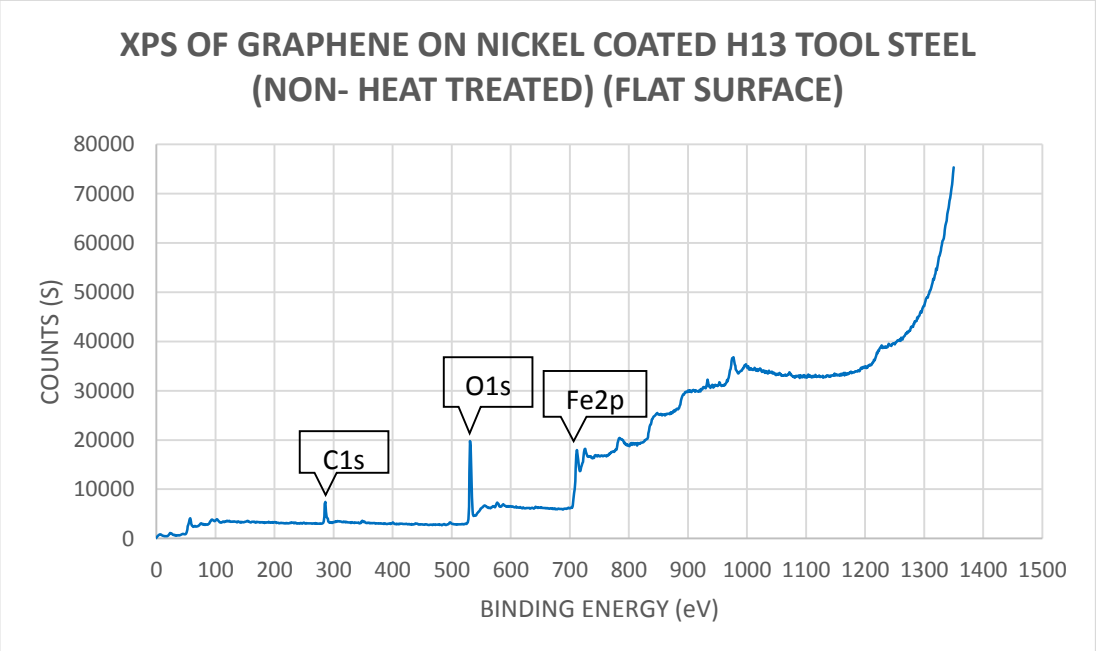

Figure 4.9: XPS of graphene on the flat surface of nickel coated H13 tool steel.

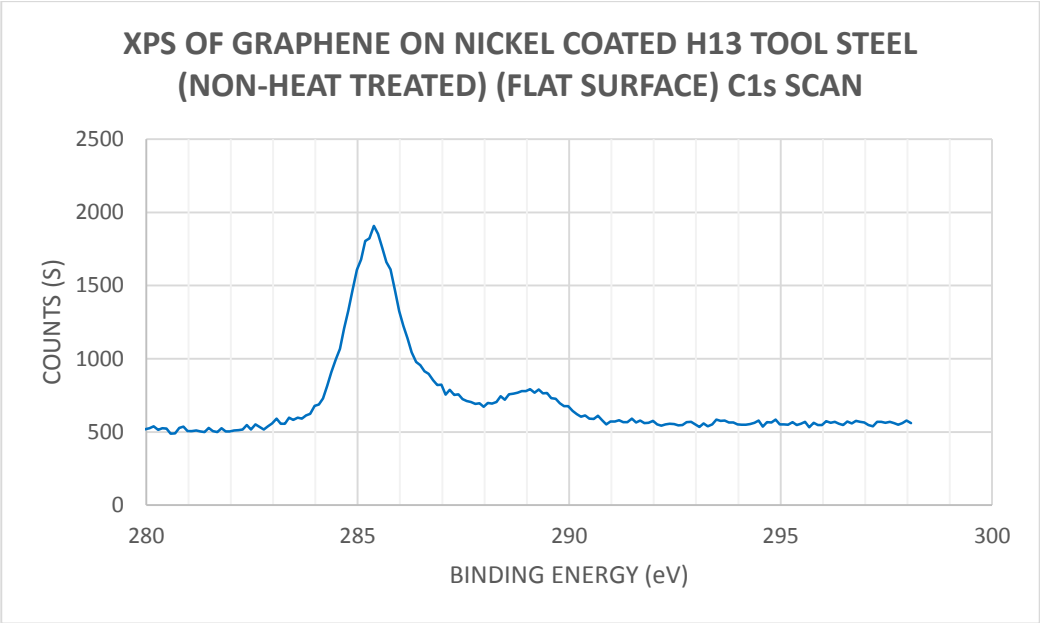

Figure 4.10: C1s XPS scan of graphene on the flat surface of nickel coated H13 tool steel.

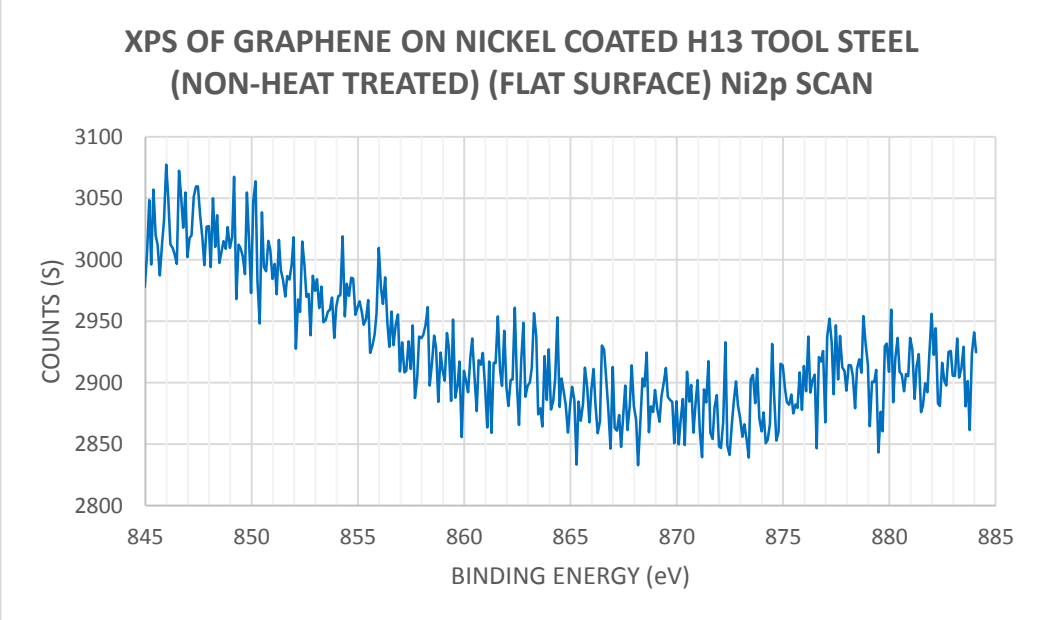

Figure 4.11: Ni2p XPS scan of graphene on the flat surface of nickel coated H13 tool steel.

Table 4.6: Tabulated data for XPS of graphene on flat surface of Ni coated H13 tool steel.

Element (Shell)	Start BE	Peak BE	End BE	Height Counts	FWHM eV	Area (P) CPS.eV	Area (N)	At. %
O1s	537.58	531.44	524.58	15383	3.62	59368	330.08	47.59
Fe2p	740.08	711.82	699.58	8465	5.72	95152	107.03	15.43
C1s	297.08	285.92	280.08	4049.7	3.08	16896	239.95	34.6
Ni2p	-	-	-	-	-	-	-	-

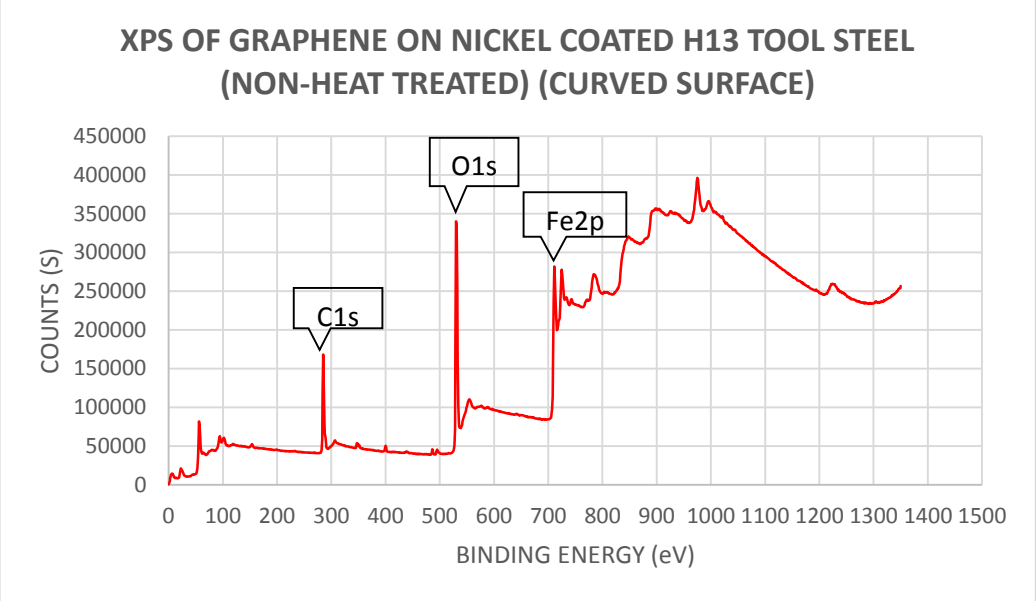

Figure 4.12: XPS of graphene on the curved surface of nickel coated H13 tool steel.

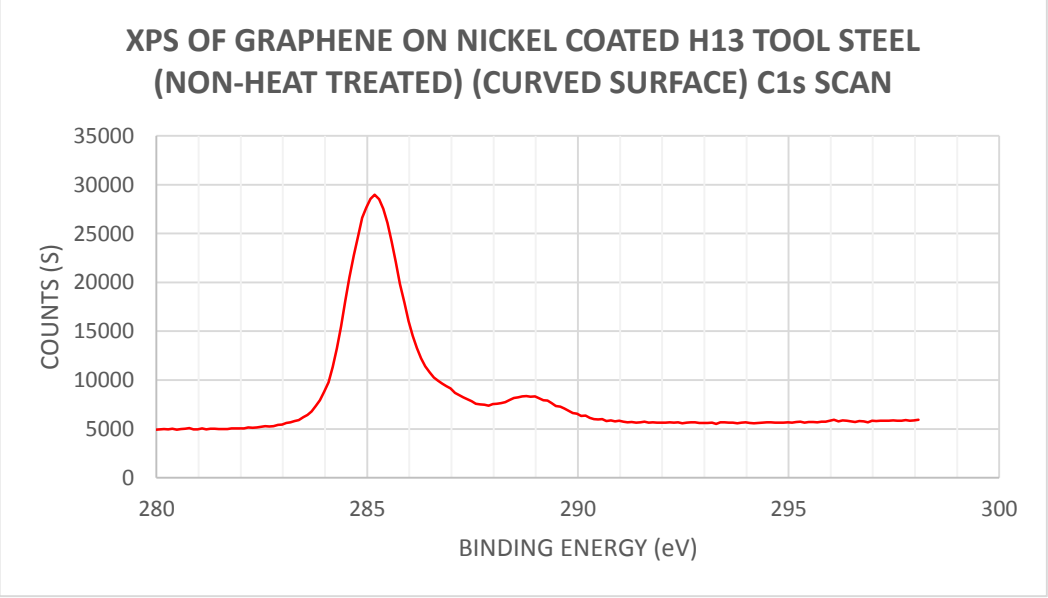

Figure 4.13: C1s XPS scan of graphene on the curved surface of nickel coated H13 tool steel.

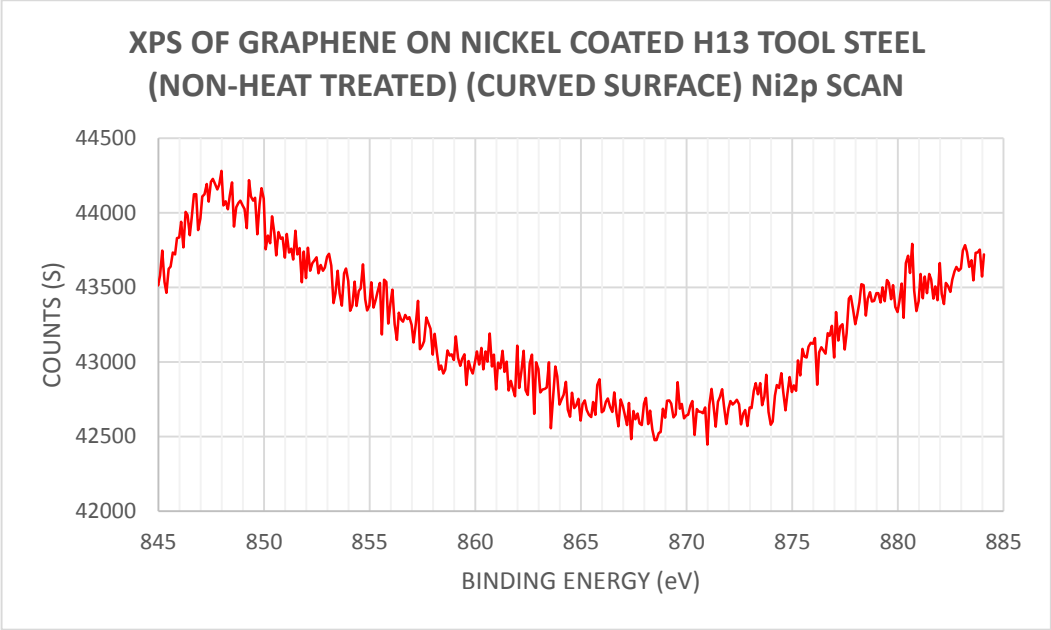

Figure 4.14: Ni2p XPS scan of graphene on the curved surface of nickel coated H13 tool steel.

Table 4.7: Tabulated data for XPS of graphene on curved surface of nickel coated H13 tool steel.

Element (Shell)	Start BE	Peak BE	End BE	Height Counts	FWHM eV	Area (P) CPS.eV	Area (N)	At. %
O1s	538.58	530.84	523.08	276178	3.5	1053702	5856.3	39.9
Fe2p	739.08	711.38	698.58	161793	4.73	1579801	1776.4	12.1
C1s	293.58	285.16	277.08	109481	2.89	379781	5391.3	36.73
Ni2p	-	-	-	-	-	-	-	-

Figure 4.9 illustrates the XPS survey spectra of graphene on nickel coated H13 tool steel at the flat surface while Figure 4.12 illustrates the XPS survey spectra of graphene on nickel coated H13 tool steel at the curved surface. From Figure 4.9 and 4.12, three prominent peaks are determined to be of O1s, C1s, and Fe2p similar to that of graphene on bare H13 tool steel. Though, it should be noted that the peaks for XPS of graphene on the flat surface of nickel coated H13 tool steel is relatively lower in comparison to the curved surface of nickel coated H13 tool steel. Both flat and curved surfaces show C1s peak at a binding energy of 285.92 eV and 285.16 eV respectively which are consistent with literatures, and proves the covalent sp^2 hybridization of carbon, and the hexagonal lattice structure of carbon [23] [30] [29]. A detailed view of the C1s peak

of both flat and curved surface are illustrated by Figure 4.10 and Figure 4.13 respectively. Based on the tabulated data in Table 4.4 and Table 4.5, for the flat surface, there has a lower C1s atomic percentage at 34.6%, in comparison the curved surface which has a C1s atomics percentage at 36.73%.

There is a discrepancy with the data obtained from XPS because it does not show any significant peak for nickel element for both flat (Figure 4.11) and curved surface (Figure 4.14). This is because there should be a peak at position 870 for photon ejected from the L_2 $2p_{1/2}$ shell or 852.7 for photon ejected from L_3 $2p_{3/2}$ shell. In addition to that, based on the XPS data tabulated in Table 4.6 and Table 4.7 the XPS scan does not pick up any significant atomic percentage of nickel, but has picked up significant atomic percentage of iron even though nickel was allegedly coated on top of it. It can be hypothesized that nickel has not been coated properly during the sputtering process or nickel has been physically removed from the substrate during the chemical vapour deposition process.

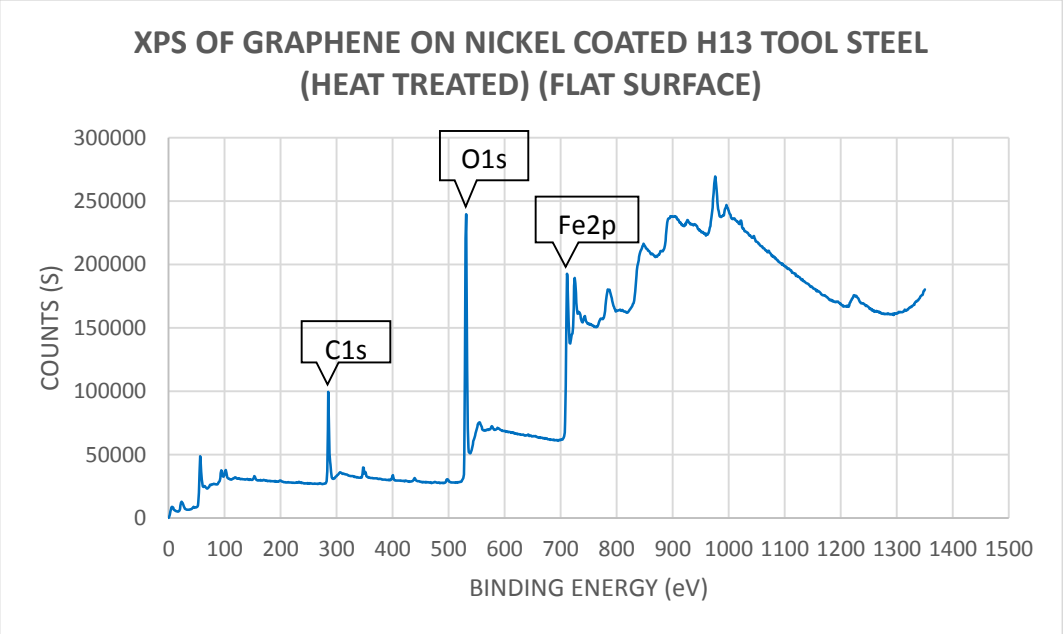

Figure 4.15: XPS of graphene on the flat surface of nickel coated heat treated H13 tool steel.

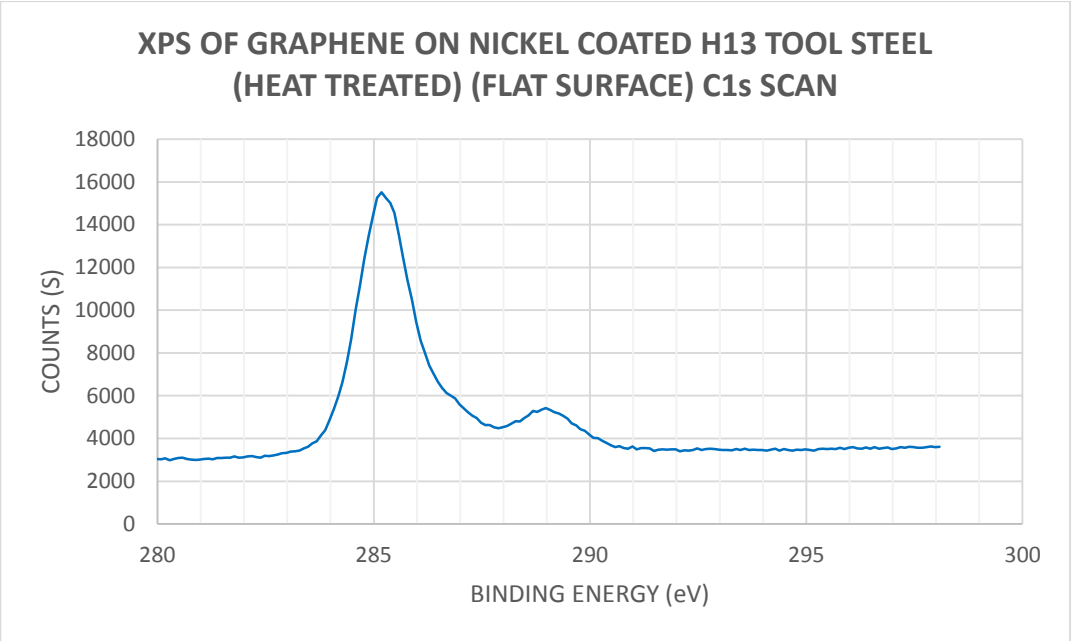

Figure 4.16: C1s XPS scan of graphene on the flat surface of nickel coated heat treated H13 tool steel.

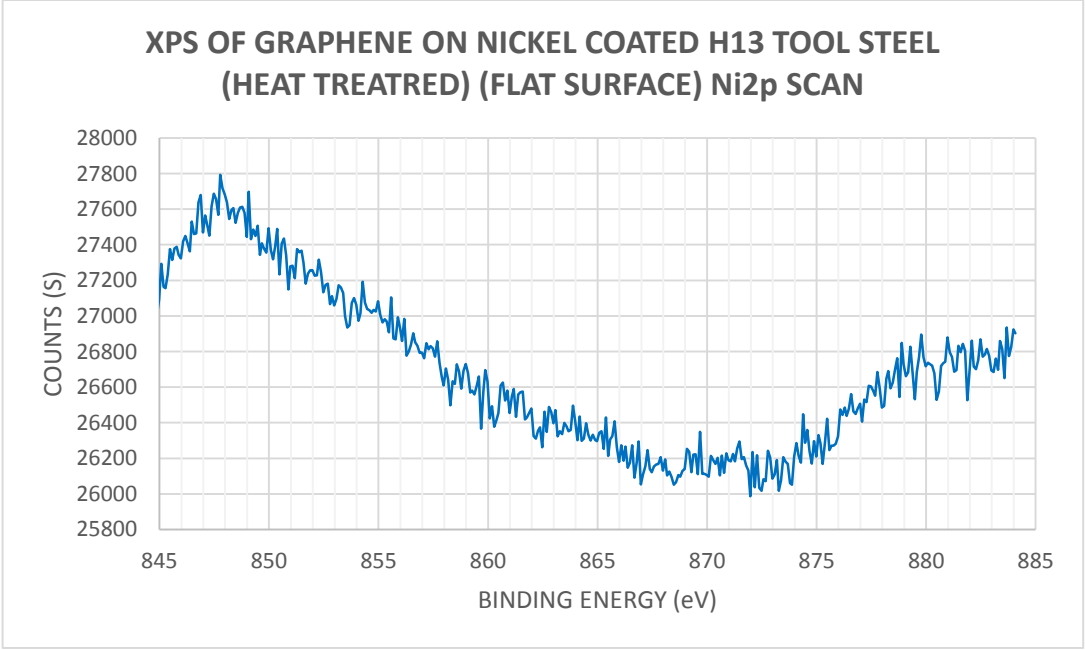

Figure 4.17: C1s XPS scan of graphene on the flat surface of nickel coated heat treated H13 tool steel.

Table 4.8: Tabulated data for XPS of graphene on flat surface of nickel coated heat treated H13 tool steel.

Element (Shell)	Start BE	Peak BE	End BE	Height Counts	FWHM eV	Area (P) CPS.eV	Area (N)	At. %
O1s	538.58	530.96	523.08	194976	3.47	728042	4046.6	42.81
Fe2p	739.08	711.38	698.58	110712	4.66	1100008	1237	13.09
C1s	294.08	285.19	277.58	62120	2.93	224152	3182.1	33.69
Ni2p	-	-	-	-	-	-	-	-

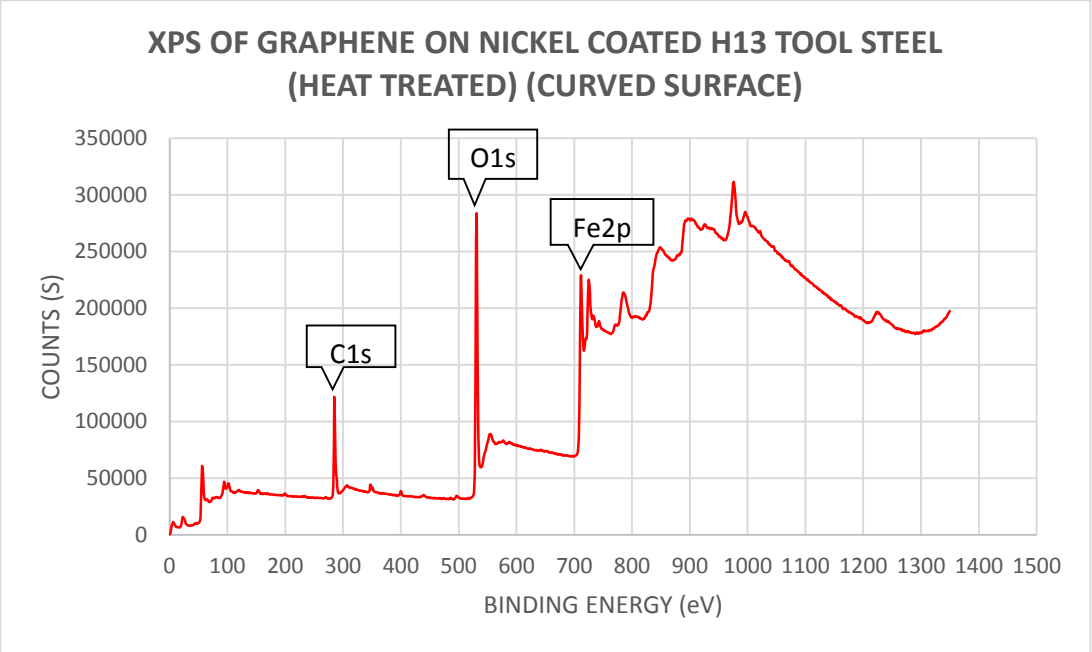

Figure 4.18: XPS of graphene on the curved surface of nickel coated heat treated H13 tool steel.

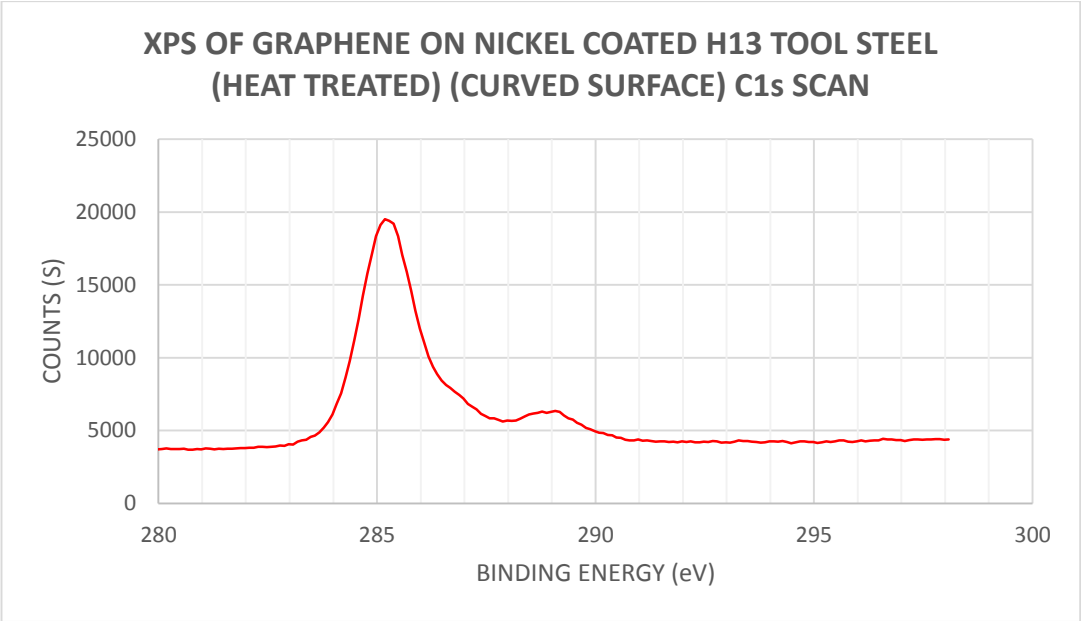

Figure 4.19: C1s XPS scan of graphene on the curved surface of nickel coated heat treated H13 tool steel.

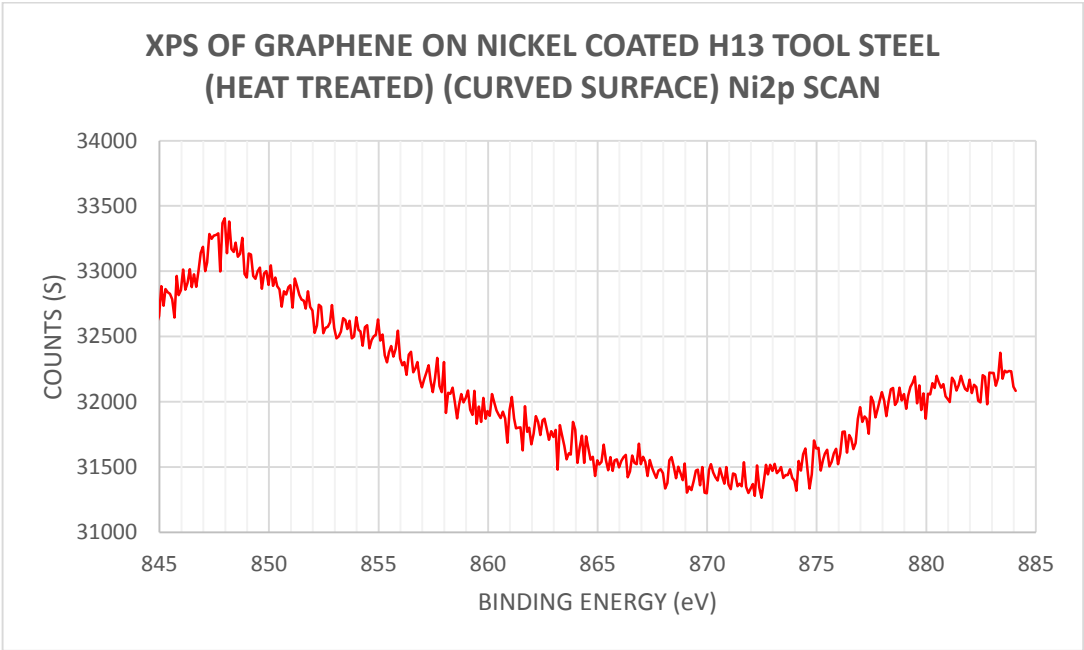

Figure 4.20: Ni2p XPS scan of graphene on the curved surface of nickel coated heat treated H13 tool steel.

Table 4.9: Tabulated data for XPS of graphene on curved surface of nickel coated heat treated H13 tool steel.

Element (Shell)	Start BE	Peak BE	End BE	Height Counts	FWHM eV	Area (P) CPS.eV	Area (N)	At. %
O1s	539.08	531.01	523.08	232814	3.51	881408	4899.2	42.23
Fe2p	740.08	711.56	699.08	134176	3.08	1333558	1499.7	12.93
C1s	294.08	285.26	277.58	77620	2.95	279813	3972.4	34.24
Ni2p	-	-	-	-	-	-	-	-

Figure 4.15 illustrates the XPS survey spectra of graphene on nickel coated heat treated H13 tool steel at the flat surface while Figure 4.18 illustrates the XPS survey spectra of graphene on nickel coated heat treated H13 tool steel at the curved surface. From Figure 4.15 and 4.18, three prominent peaks are determined to be of O1s, C1s, and Fe2p similar to that of graphene on bare H13 tool steel and nickel coated H13 tool steel (non-heat treated). The intensities of the O1s, C1s and Fe2p peaks are similar for both flat and curved surface. Both flat and curved surfaces show C1s peak at a binding energy of 285.19 eV and 285.26 eV respectively which are consistent with literatures, and proves the covalent sp^2 hybridization of carbon, and the hexagonal lattice structure of carbon [23] [30] [29]. A detailed view of the C1s peak of both flat and curved surface are illustrated by Figure 4.16 and Figure 4.19 respectively. Based on the tabulated data in Table 4.4 and Table 4.5, for the flat surface, there has a lower C1s atomic percentage at 33.69%, in comparison the curved surface which has a C1s atomics percentage at 34.24%.

Similar to the earlier discussion for the nickel coated H13 tool steel (non-heat treated) substrate, this substrate does not show any significant peak for nickel element for both flat (Figure 4.17) and curved surface (Figure 4.20). In addition to that, the XPS data tabulated in Table 4.8 and Table 4.9 show that the XPS scan did not pick up any trace of nickel element. The same hypothesis can be made for these data where nickel may not have been coated properly during the sputtering process or nickel has been physically removed from the substrate during the chemical vapour deposition process.

4.3 FE-SEM and EDS

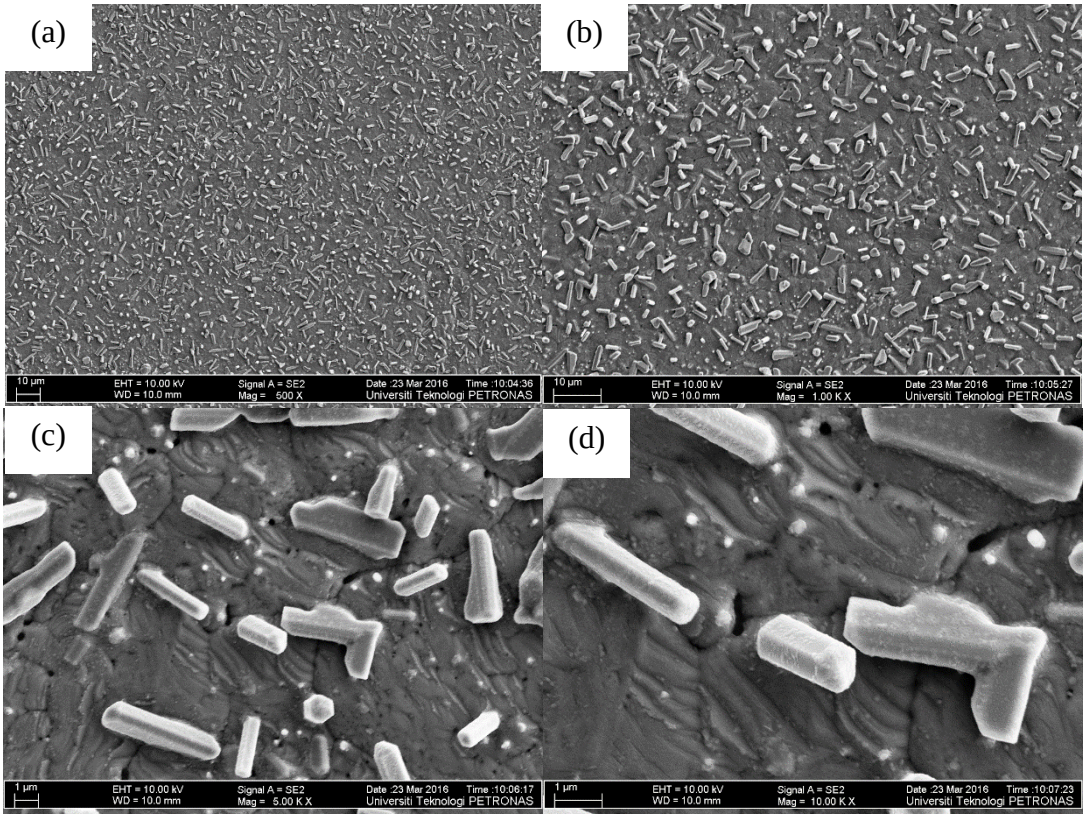

Figure 4.21: SEM imaging of graphene coated on bare H13 tool steel at magnification of (a) 500 X (b) 1000 X (c) 5000 X and (d) 10000X.

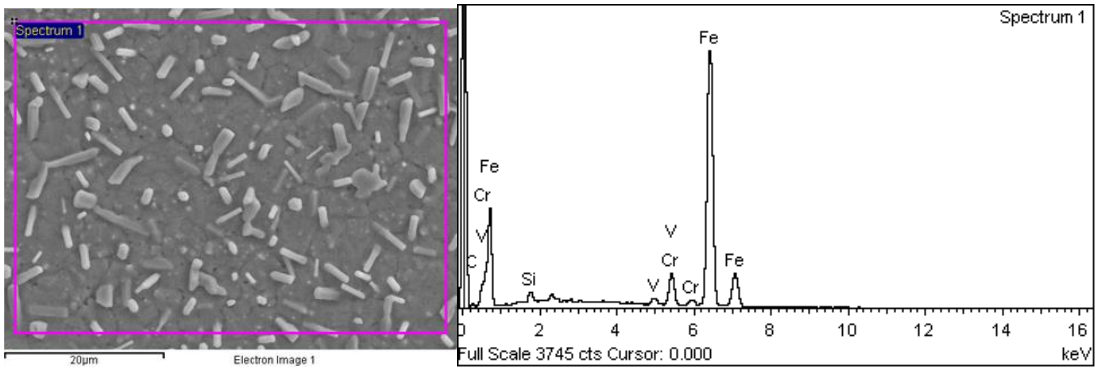

Figure 4.22: Region EDX scan (left) and EDX elemental graph (right) of graphene coated H13 tool steel.

Table 4.10: Elemental percentage of region scan based on Figure 4.22.

Element	Weight %	Atomic %
C	5.92	22.33
Si	1.17	1.89
V	1.17	1.04
Cr	5.91	5.14
Fe	85.83	69.60

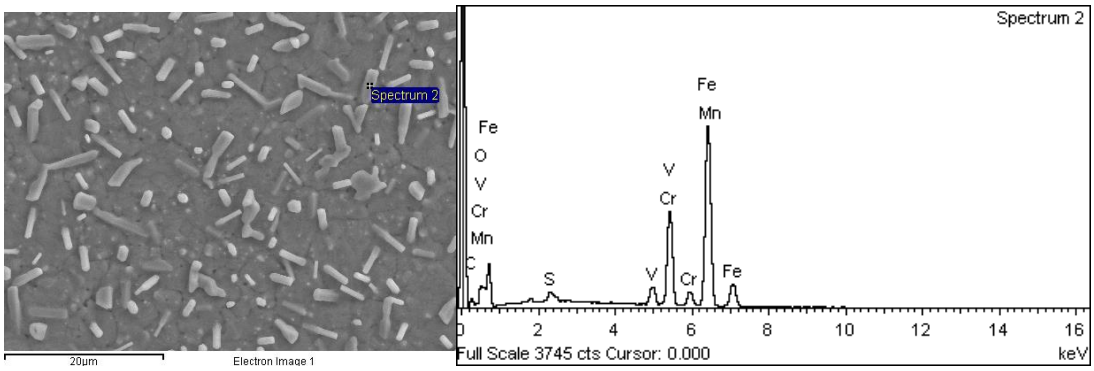

Figure 4.23: Spot EDX scan of the graphitic structure (left) and EDX elemental graph of the graphitic structure (right) on graphene coated H13 tool steel.

Table 4.11: Elemental percentage of the graphitic structure based on Figure 4.23.

Element	Weight %	Atomic %
C	9.44	30.22
O	3.40	8.17
S	0.72	0.86
V	3.58	2.70
Cr	19.91	14.71
Mn	0.95	0.67
Fe	62.00	42.67

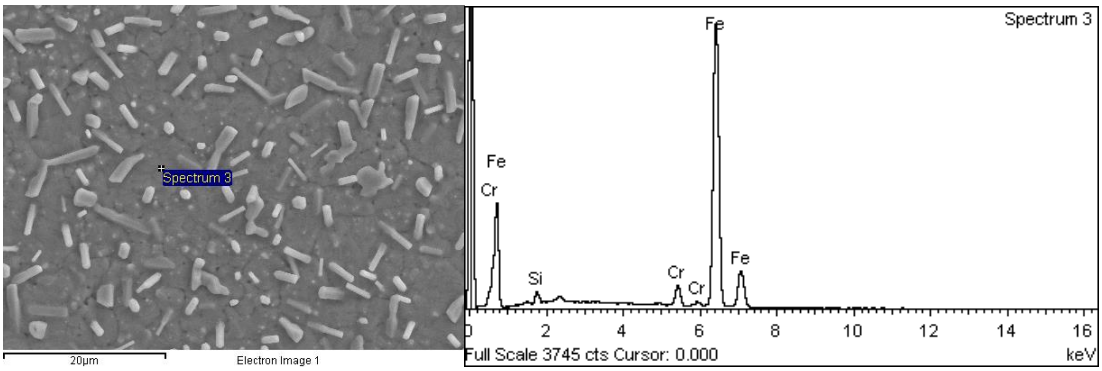

Figure 4.24: Spot EDX scan of the surface (left) and EDX elemental graph of the surface (right) on graphene coated H13 tool steel.

Table 4.12: Elemental percentage of the surface based on Figure 4.24.

Element	Weight %	Atomic %
Si	1.36	2.66
Cr	3.56	3.76
Fe	95.08	93.57

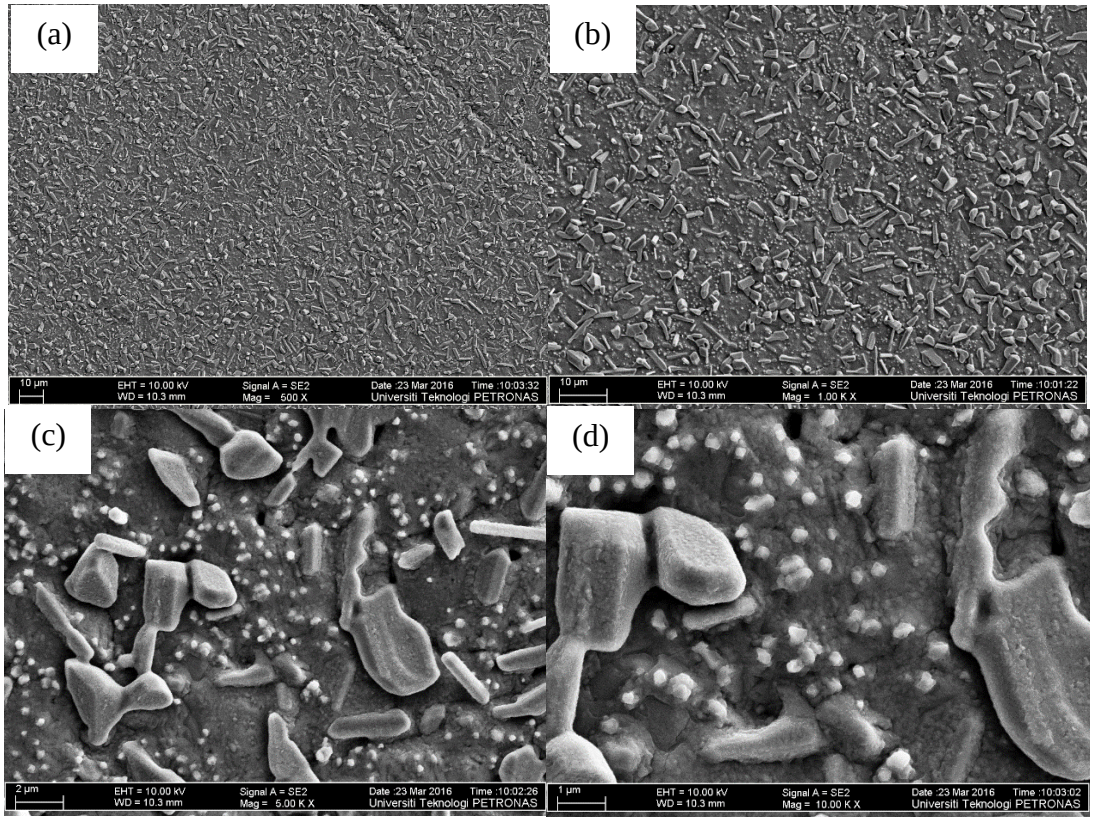

Figure 4.25: SEM imaging of graphene coated on allegedly nickel coated H13 tool steel at magnification of (a) 500 X (b) 1000 X (c) 5000 X and (d) 10000X.

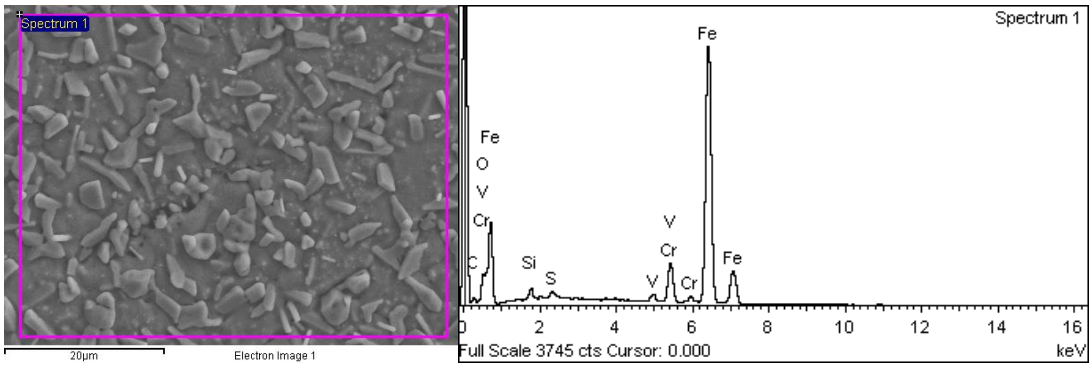

Figure 4.26: Region EDX scan (left) and EDX elemental graph (right) of graphene coated on allegedly nickel coated H13 tool steel.

Table 4.13: Elemental percentage of region scan based on Figure 4.26.

Element	**Weight %**	**Atomic %**
C	7.32	24.29
O	4.58	11.41
Si	0.93	1.32
S	0.56	0.70
V	1.21	0.95
Cr	6.85	5.25
Fe	78.54	56.07

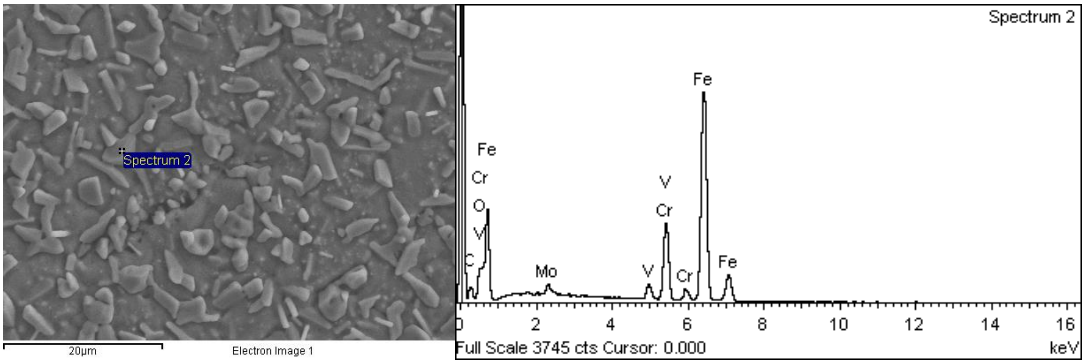

Figure 4.27: Spot EDX scan of the graphitic structure (left) and EDX elemental graph of the graphitic structure (right) on graphene coated allegedly nickel coated H13 tool steel.

Table 4.14: Elemental percentage of region scan based on Figure 4.27.

Element	Weight %	Atomic %
C	7.31	24.25
O	2.98	9.67
V	2.90	2.95
Cr	16.39	16.33
Fe	67.68	45.32
Mn	2.73	1.47

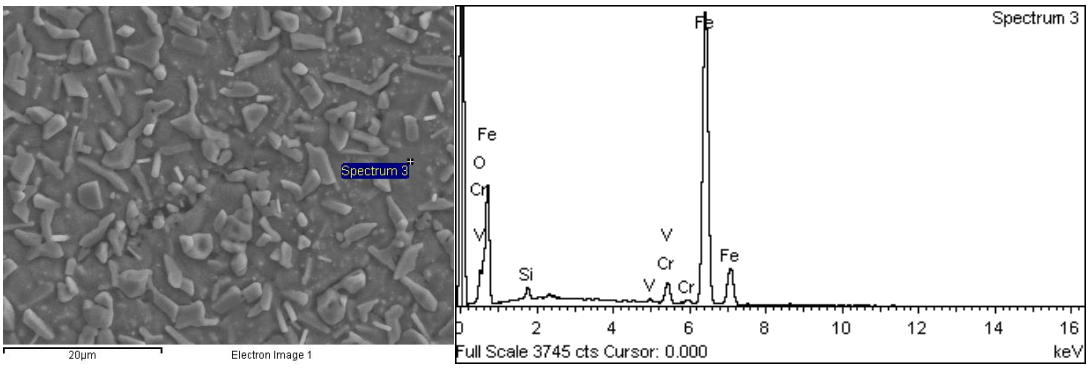

Figure 4.28: Spot EDX scan of the surface (left) and EDX elemental graph of the surface (right) of graphene coated allegedly nickel coated H13 tool steel.

Table 4.15: Elemental percentage of the surface based on Figure 4.28.

Element	Weight %	Atomic %
O	4.69	14.48
Si	1.15	2.02
V	0.43	0.42
Cr	3.53	3.35
Fe	90.20	79.73

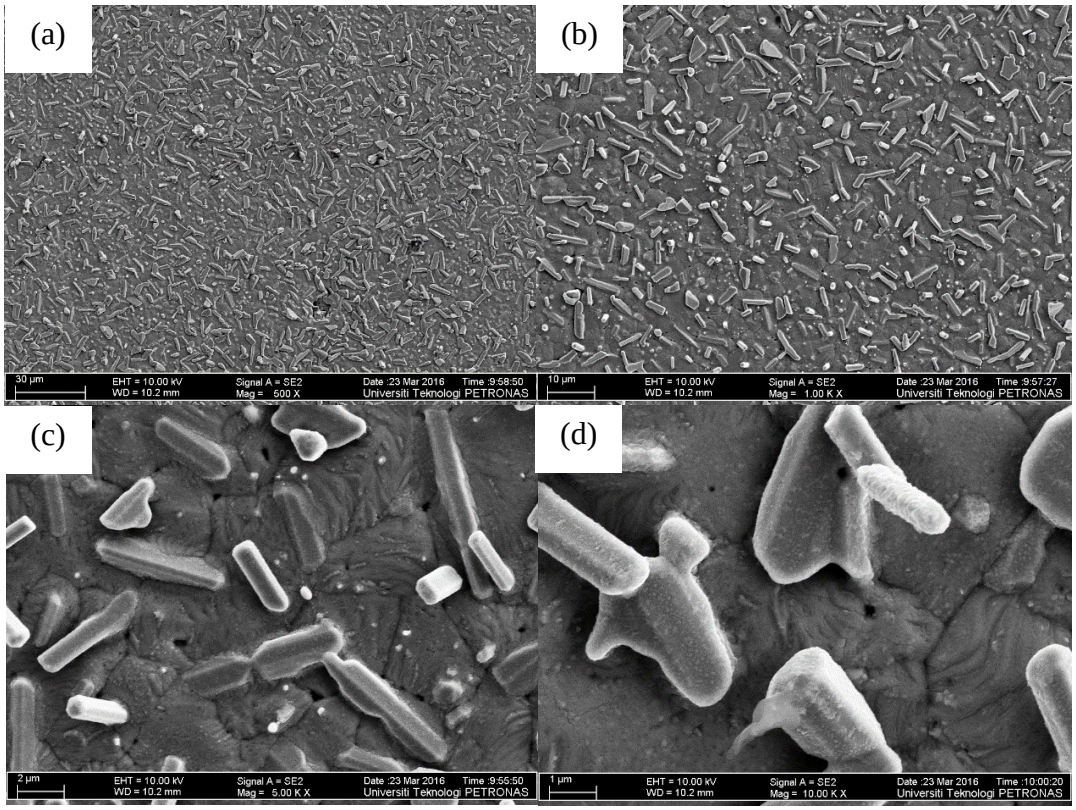

Figure 4.29: SEM imaging of graphene coated on allegedly nickel coated heat treated H13 tool steel at magnification of (a) 500 X (b) 1000 X (c) 5000 X and (d) 10000X.

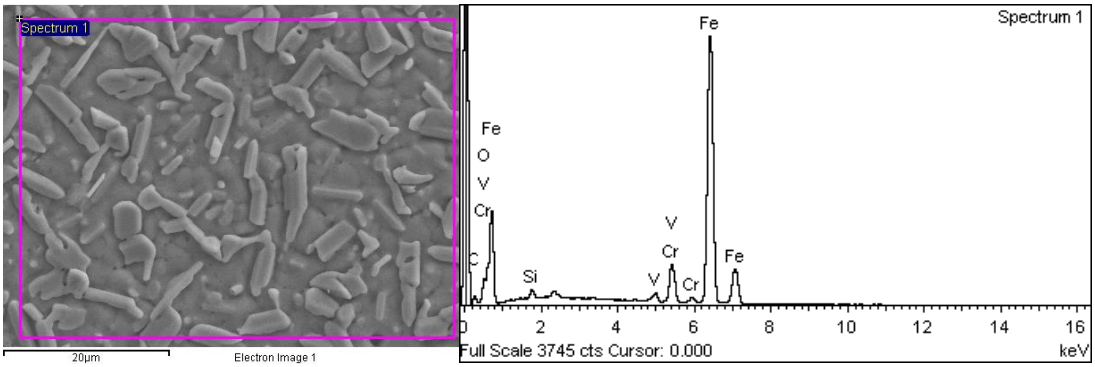

Figure 4.30: Region EDX scan (left) and EDX elemental graph (right) of graphene coated on allegedly nickel coated heat treated H13 tool steel.

Table 4.16: Elemental percentage of region scan based on Figure 4.30.

Element	Weight %	Atomic %
C	7.63	25.66
O	3.59	9.08
Si	0.83	1.20
V	1.17	0.93
Cr	6.47	5.03
Fe	80.31	58.11

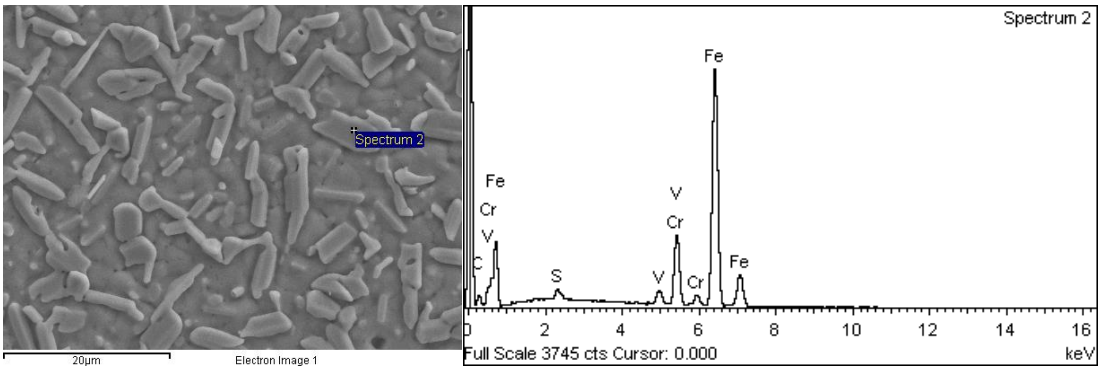

Figure 4.31: Spot EDX scan of the graphitic structure (left) and EDX elemental graph of the graphitic structure (right) on graphene coated allegedly nickel coated heat treated H13 tool steel.

Table 4.17: Elemental percentage of region scan based on Figure 4.31.

Element	Weight %	Atomic %
C	11.02	36.11
S	0.71	0.88
V	2.38	1.84
Cr	13.01	9.85
Fe	72.87	51.33

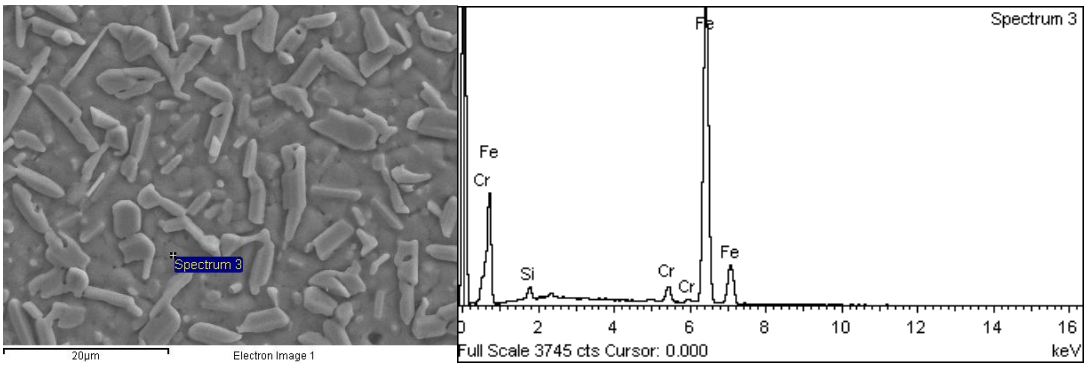

Figure 4.32: Spot EDX scan of the surface (left) and EDX elemental graph of the surface (right) of graphene coated allegedly nickel coated heat treated H13 tool steel.

Table 4.18: Elemental percentage of the surface based on Figure 4.32.

Element	Weight %	Atomic %
Si	1.47	2.87
Cr	2.85	3.01
Fe	95.68	94.12

Figure 4.21, Figure 4.25, and Figure 4.29 are SEM imaging of graphene coated on bare H13 tool steel (1st sample), graphene coated on nickel coated H13 tool steel (2nd sample), and graphene coated on nickel coated heat treated H13 tool steel (3rd sample) respectively. At a magnification of 10 000 times, all the samples show the same type of crystal like deposition on the surface of the substrate. These results were in contrary to researches because no graphene formations resembling Figure A4. In addition to that, these crystal like structures were never reported in any journals.

To determine the elemental composition of the crystal like structure as well as the reason behind the absence of graphene, EDS was carried out. A wide regional scan was done to roughly determine the general composition of the surface of the samples as depicted by Figure 4.22, Figure 4.26, and Figure 4.30. Table 4.10, Table 4.13, and Table 4.16 were tabulated based on the EDS elemental graph of the aforementioned figures. All three regional EDS revealed similar results where the weight percentage of carbon element is between 5% to 8%. There was presence of oxygen which may be due to the oxidation of the H13 tool steel substrate. Similar to the XPS experiment conducted, nickel element was absent for both nickel coated substrates which could

hint to be the reason behind the absence of graphene. Other elements such as chromium and vanadium were present which is due to the alloy composition of H13 tool steel.

To determine the exact composition of the crystal structure, spot EDS scans were done on crystal like structure of all three samples as depicted by Figure 4.23, Figure 4.27, and Figure 4.31. Table 4.11, Table 4.14, and Table 4.17 were tabulated based on the spot EDS elemental graph of the aforementioned figures. All three samples show 3 distinct elements which are carbon, chromium, and iron each making up 7% to 9%, 6% to 19%, and 62% to 72% respectively. These values were compared to the spot EDS scan of the surface of the samples as depicted by Figure 4.24, Figure 4.28, and Figure 4.32. Table 4.12, Table 4.15, and Table 4.18 were tabulated based on the spot EDS elemental graph of the sample surfaces. From the spot EDS of the samples surfaces, no traces of carbon element were found. However, chromium and iron were found at a weight percentage range of 2% to 4%, and 90% to 96% respectively. From this, it can be concluded that that the crystal like structure is probably made of carbon and therefore graphitic in nature.

4.4 Effect of Heat-Treatment on Graphene Synthesis

From the Raman spectra, the results obtained for the heat treated and non-heat treated samples were similar. This is based on the similar D peak, G peak and 2D peak. In addition to that, the intensity of graphene characteristic G and 2D peaks were similar as they resulted in an I_G/I_{2D} ratio of greater than 1 which suggests for multi-layered graphene growth. The XPS characterization of the surface revealed similar results for both heat treated and non-heat treated samples. Both samples revealed an atomic percentage of carbon at a range of 30% to 40%. In addition to that, both samples revealed distinct peak for C1s which suggests for the existence of carbon-carbon bonds which is characteristic of graphene. FE-SEM and EDS both revealed that the heat treated and non-heat treated samples did not reveal any graphene layers but revealed same crystal like structures. These crystal like structures were revealed to be of graphitic nature as the EDS revealed high percentage of carbon.

One inference for non-difference between heat treated and non-heat treated samples is that the working temperature of the chemical vapour deposition process of 1000°C to

25°C has annealed the heat treated sample. 1010°C is the austenizing region of H13 tool steel [38]. Since the working temperature of the CVD process close to the austenizing region, the heat treated substrate which has martensitic structures are converted to austenitic structures by the process of annealing. This annealing process releases the internal stress caused by martensitic structures and allows for an even distribution of carbon atoms in H13 tool steel. With the formation of austenitic structure during the CVD process, both the heat treated and non-heat treated substrates are considered to be identical to each other.

4.5 Inference of Graphene Absence

From the poor Raman spectroscopy intensity, field-emission scanning electron microscopy, and electron dispersive spectroscopy, it can be concluded that graphene was not present in any of the samples. The first inference of graphene absence is that the CVD parameters that were applied to synthesize graphene were meant for nickel substrate instead on H13 tool steel substrate. Since no nickel coating were present on the surface of H13 tool steel, therefore the CVD process were carried on H13 tool steel. Experiment conducted by [23] made use of ethanol as the CVD precursor with a reaction time of 15 minutes for synthesis of graphene directly on stainless steel. In addition to that, modified carburization process was used by [28] to synthesize graphene on directly on stainless steel. These graphene synthesis techniques were different to the technique used in this report where the CVD process precursor was methane with a reaction time of 20 minutes. The volume, surface area, and type of the substrate also could have played a role in the synthesis of graphene as the rate of cooling of the substrate is significant in the formation of hexagonal graphene structures [23] [28]. H13 tool steel which has a thermal conductivity of 24.7 W/m-K is able to cool faster in comparison to SS316L stainless steel with a thermal conductivity of 21.4 W/m-K [6] [42]. Although, the difference may not be significant, but even the slightest change in the rate of cooling can affect the synthesis of carbon as reported by [23].

The absence of nickel coating on H13 tool steel is significant. This is because nickel has been reported to be a very good catalyst for the synthesis of graphene [21]. The nickel coating for H13 tool steel was conducted in a magnetron sputtering machine. Observation during the nickel coating process revealed an intermittent nickel

sputtering in which the DC-gun would turn on and off and irregular intervals. The nickel coating process was conducted thrice, and all three revealed similar intermittent nickel sputtering process.

CHAPTER 5
CONCLUSION AND RECOMMENDATION

5.1 Conclusion

From the results obtained from Raman Spectroscopy, X-ray Photoelectron Spectroscopy and Scanning Electron Microscopy together with Electron Dispersive Spectroscopy, it can be concluded that graphene was not synthesized on the surface of H13 tool steel. This is in spite of the near positive results for graphene growth obtained from Raman Spectroscopy, and X-ray Photoelectron Spectroscopy. Visual inspection using the Scanning Electron Microscopy proved that there were no graphene formations, however graphitic crystal like structures were observed. In addition to that, the effect of heat-treatment on synthesis of epitaxial graphene was non-existent as both the non-heated and heat treated substrate revealed the same results for Raman Spectroscopy, X-ray Photoelectron as well as the Scanning Electron Microscopy.

5.2 Recommendations

To allow for better results in the future, several key obstacles should be highlighted and overcome. The first obstacle in this project was the Magnetron Sputtering of nickel onto the H13 tool steel. As revealed in the results, no trace of nickel element was detected. This was due to problems with Magnetron Sputtering having an intermittent problem whenever H13 tool steel was involved. In future experiments, if Magnetron Sputtering is selected as the coating method nickel, the intermittent problem should be rectified. Proper nickel coating will proper catalytic action of nickel to synthesize epitaxial graphene. The next key obstacle is obtaining proper parameters for the Chemical Vapour Deposition. This is because no research has been done on chemical vapour depositing graphene on H13 tool steel as the substrate. Most of the existing research are focused towards the coating graphene on bare stainless steel

instead of H13 tool steel. In addition to that, parameters for graphene synthesis through Chemical Vapour Deposition should be address the effect of thermal conductivity of substrate. Thermal conductivity is closely related to the rate of cooling of the substrate which affects the synthesis of graphene during the Chemical Vapour Deposition process.

CHAPTER 6

REFERENCES

[1] R. Mishra and Z. Ma, "Friction stir welding and processing," *Materials Science and Engineering: R: Reports,* vol. 50, no. 1–2, pp. 1-78, 2005.

[2] R. S. Mishra and M. W. Mahoney, "Introduction," in *Friction stir welding and processing*, ASM international, 2007.

[3] Á. Meilinger and I. Török, "The importance of friction stir welding tool," *Production Processes and Systems,* vol. 6, pp. 25-34.

[4] C. B. Fuller, "Friction Stir Tooling: Tool Materials and Designs," in *Friction Stir Welding and Processing*, ASM International, 2007, pp. 7-35.

[5] Y. Zhang, X. Cao, S. Larose and P. Wanjara, "Review of tools for friction stir welding and processing," *Canadian Metallurgical Quarterly,* vol. 51, no. 3, pp. 250-261, 2012.

[6] MatWeb, LLC, "AISI Type H13 Hot Work Tool Steel," MatWeb, LLC, [Online]. Available: http://www.matweb.com/search/datasheet_print.aspx?matguid=e30d1d1038164808a85cf7ba6aa87ef7. [Accessed 1 November 2015].

[7] Special Metals Corporation, "PRODUCT HANDBOOK OF HIGH–PERFORMANCE NICKEL ALLOYS," Precision Castparts Corp, [Online]. Available: http://www.specialmetals.com/assets/documents/pcc-8064-sm-alloy-handbook-v04.pdf. [Accessed 1 November 2015].

[8] Plansee, "Tungsten heavy alloys," The Plansee Group, [Online]. Available: http://www.plansee.com/en/materials/tungsten-heavy-metal.html. [Accessed 1 November 2015].

[9] C. D Sorenson and T. W Nelson, "Friction Stir Welding of Ferrous and Nickel Alloys," in *Friction Stir Welding and Processing*, ASM International, 2007, pp. 111-121.

[10] T. K. Harris, E. J. Brookes and C. J. Taylor, "The effect of temperature on the hardness of polycrystalline cubic boron nitride cutting tool materials," *International Journal of Refractory Metals and Hard Materials,* vol. 22, no. 2-3, pp. 105-110, 2004.

[11] D. Hansora, N. Shimpi and S. Mishra, "Graphite to Graphene via Graphene Oxide: An Overview on Synthesis, Properties, and Applications," *JOM,* pp. 1-14, 2015.

[12] F. Liu, P. Ming and J. Li, "Ab initio calculation of ideal strength and phonon instability of graphene under tension," *Physical Review B,* vol. 76, no. 6, p. 064120, 2007.

[13] C. Lee, X. Wei, J. W. Kysar and J. Hone, "Measurement of the elastic properties and intrinsic strength of monolayer graphene," *science,* vol. 321, no. 5887, pp. 385-388, 2008.

[14] I. Ovid'ko, "Mechanical properties of graphene," *Rev. Adv. Mater. Sci.,* vol. 34, pp. 1-11, 2013.

[15] J. M. Garcia, R. He, M. P. Jiang, P. Kim, L. N. Pfeiffer and A. Pinczuk, "Multilayer graphene grown by precipitation upon cooling of nickel on diamond," *Carbon,* vol. 49, no. 3, pp. 1006-1012, 2011.

[16] L. L. Patera, C. Africh, R. S. Weatherup, R. Blume, S. Bhardwaj, C. Castellarin-Cudia, A. Knop-Gericke, R. Schloegl, G. Comelli and S. Hofmann, "In situ observations of the atomistic mechanisms of Ni catalyzed low temperature graphene growth," *ACS nano,* vol. 7, no. 9, pp. 7901-7912, 2013.

[17] Y. Shamoto and M. Aoki, "Adsorption, bond formation and graphitization of carbon atoms on Ni (111) surface," *Materials transactions,* vol. 47, no. 11, pp. 2674-2677, 2006.

[18] A. Dahal and M. Batzill, "Graphene–nickel interfaces: a review," *Nanoscale,* vol. 6, no. 5, pp. 2548-2562, 2014.

[19] B. G. Priyadarshini, S. Aich and M. Chakraborty, "Structural and morphological investigations on DC-magnetron-sputtered nickel films deposited on Si (100)," *Journal of materials science,* vol. 46, no. 9, pp. 2860-2873, 2011.

[20] E. Loginova, N. Bartelt, P. Feibelman and K. McCarty, "Factors influencing graphene growth on metal surfaces," *New Journal of Physics,* vol. 11, no. 6, p. 063046, 2009.

[21] C. Miao, C. Zheng, O. Liang and Y.-H. Xie, Chemical vapor deposition of graphene, INTECH Open Access Publisher, 2011.

[22] Z. Ni, Y. Wang, T. Yu and Z. Shen, "Raman spectroscopy and imaging of graphene," *Nano Research,* vol. 1, no. 4, pp. 273-291, 2008.

[23] R. John, A. Ashokreddy, C. Vijayan and T. Pradeep, "Single-and few-layer graphene growth on stainless steel substrates by direct thermal chemical vapor deposition," *Nanotechnology,* vol. 22, no. 16, pp. 165-701, 2011.

[24] N.-W. Pu, G.-N. Shi, Y.-M. Liu, X. Sun, J.-K. Chang, C.-L. Sun, M.-D. Ger, C.-Y. Chen, P.-C. Wang and Y.-Y. Peng, "Graphene grown on stainless steel as a high-performance and ecofriendly anti-corrosion coating for polymer electrolyte membrane fuel cell bipolar plates," *Journal of Power Sources,* vol. 282, pp. 248-256, 2015.

[25] A. C. Stoot, L. Camilli, S.-A. Spiegelhauer, F. Yu and P. Bøggild, "Multilayer graphene for long-term corrosion protection of stainless steel bipolar plates for polymer electrolyte membrane fuel cell," *Journal of Power Sources,* vol. 293, pp. 846-851, 2015.

[26] D. R. Cooper, B. D'Anjou, N. Ghattamaneni, B. Harack, M. Hilke, A. Horth, N. Majlis, M. Massicotte, L. Vandsburger and E. Whiteway, "Experimental review of graphene," *ISRN Condensed Matter Physics,* vol. 2012, 2012.

[27] M. J. Allen, V. C. Tung and R. B. Kaner, "Honeycomb carbon: a review of graphene," *Chemical reviews,* vol. 110, no. 1, pp. 132-145, 2009.

[28] H. Gullapalli, A. L. Mohana Reddy, S. Kilpatrick, M. Dubey and P. M. Ajayan, "Graphene growth via carburization of stainless steel and application in energy storage," *Small,* vol. 7, no. 12, pp. 1697-1700, 2011.

[29] Y. Xue, B. Wu, Y. Guo, L. Huang, L. Jiang, J. Chen, D. Geng, Y. Liu, W. Hu and G. Yu, "Synthesis of large-area, few-layer graphene on iron foil by chemical vapor deposition," *Nano Research,* vol. 4, no. 12, pp. 1208-1214, 2011.

[30] K. R. Paton, E. Varrla, C. Backes, R. J. Smith, U. Khan, A. O'Neill, C. Boland, M. Lotya, O. M. Istrate and P. King, "Scalable production of large quantities of defect-free few-layer graphene by shear exfoliation in liquids," *Nature materials,* vol. 13, no. 6, pp. 624-630, 2014.

[31] Z. Xu and M. J. Buehler, "Interface structure and mechanics between graphene and metal substrates: a first-principles study," *Journal of Physics: Condensed Matter,* vol. 22, no. 48, p. 485301, 2010.

[32] S. Das, D. Lahiri, D.-Y. Lee, A. Agarwal and W. Choi, "Measurements of the adhesion energy of graphene to metallic substrates," *Carbon,* vol. 59, pp. 121-129, 2013.

[33] D. Cormier, O. Harrysson and H. West, "Characterization of H13 steel produced via electron beam melting," *Rapid Prototyping Journal,* vol. 10, no. 1, pp. 35-41.

[34] L. Xiao, X. P. Su, J. Wang and Y. Zhou, "A novel blister test to evaluate the interface strength between nickel coating and low carbon steel substrate," *Materials Science and Engineering: A,* vol. 501, no. 1, pp. 235-241, 2009.

[35] R. Weil and K. Parker, "The properties of electroless nickel," *Electroless plating: fundamentals and applications,* 1990.

[36] H. Hiura, H. Miyazaki and K. Tsukagoshi, "Determination of the number of graphene layers: discrete distribution of the secondary electron intensity stemming from individual graphene layers," *Applied Physics Express,* vol. 3, no. 9, p. 095101, 2010.

[37] J. Lahiri, T. S. Miller, A. J. Ross, L. Adamska, I. I. Oleynik and M. Batzill, "Graphene growth and stability at nickel surfaces," *New Journal of Physics,* vol. 13, no. 2, p. 025001, 2011.

[38] W. E. Bryson, Heat Treatment, Selection, and Application of Tool Steels (2nd Edition), Cincinnati: Hanser Publishers, 2009.

[39] M. Farooq and Z. Lee, "Optimization of the sputtering process for depositing composite thin films," *Journal of the Korean Physical Society,* vol. 40, no. 3, pp. 511-515, 2002.

[40] Z. Chen, W. Ren, B. Liu, L. Gao, S. Pei, Z.-S. Wu, J. Zhao and H.-M. Cheng, "Bulk growth of mono-to few-layer graphene on nickel particles by chemical vapor deposition from methane," *Carbon,* vol. 48, no. 12, pp. 3543-3550, 2010.

[41] Graphene Supermarket, "Frequently Asked Questions about Graphene Grown via Chemical Vapor Deposition," [Online]. Available: http://graphene-supermarket.com/White_Papers/CVDGrapheneFAQ.pdf. [Accessed 27 December 2015].

[42] AK Steel Corporation, "Product Data Sheet 316/316L Stainless Steel," 2007. [Online]. Available: http://www.aksteel.com/pdf/markets_products/stainless/austenitic/316_316l_data_sheet.pdf. [Accessed 6 April 2016].

CHAPTER 7

APPENDICES

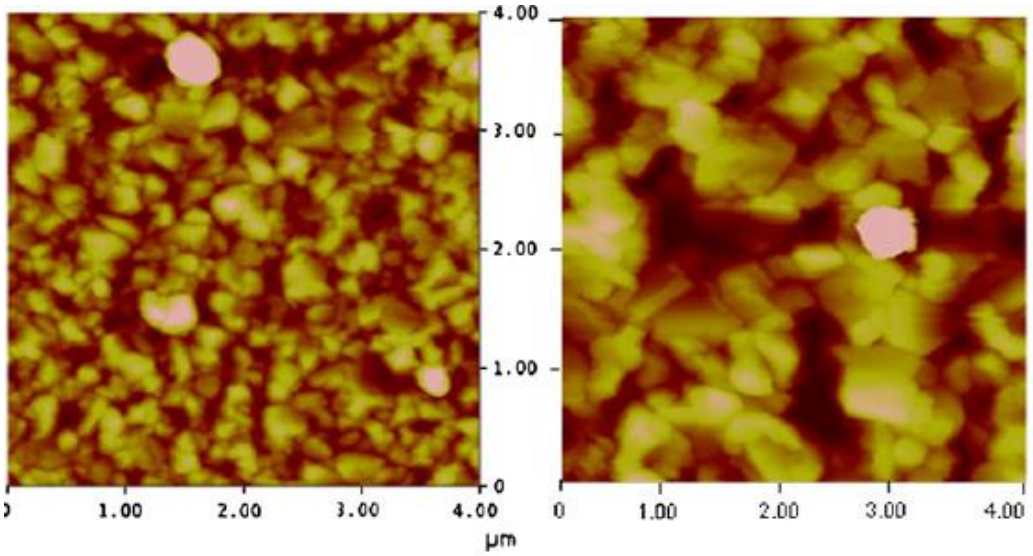

Figure A1: AFM image of nickel deposited at 570K (left) and 770K (right)

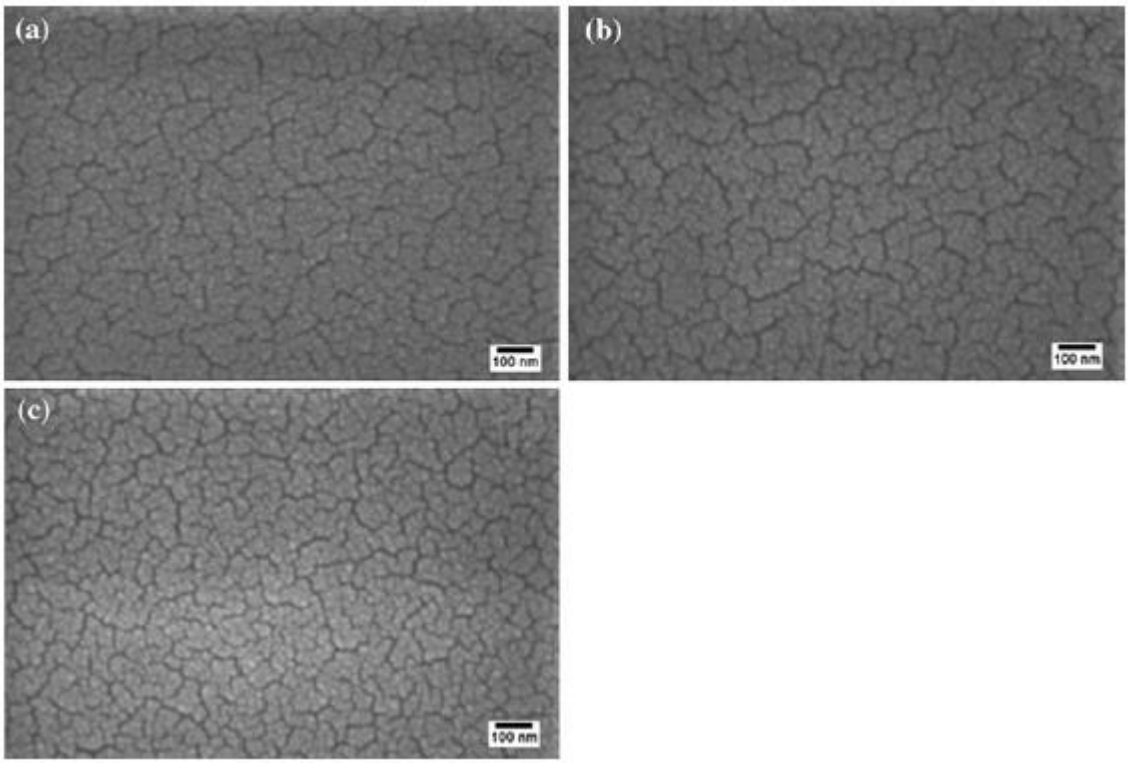

Figure A2: Planar FE-SEM image of nickel deposited at 10mTorr (image a), 15mTorr (image b), 20mTorr (image c)

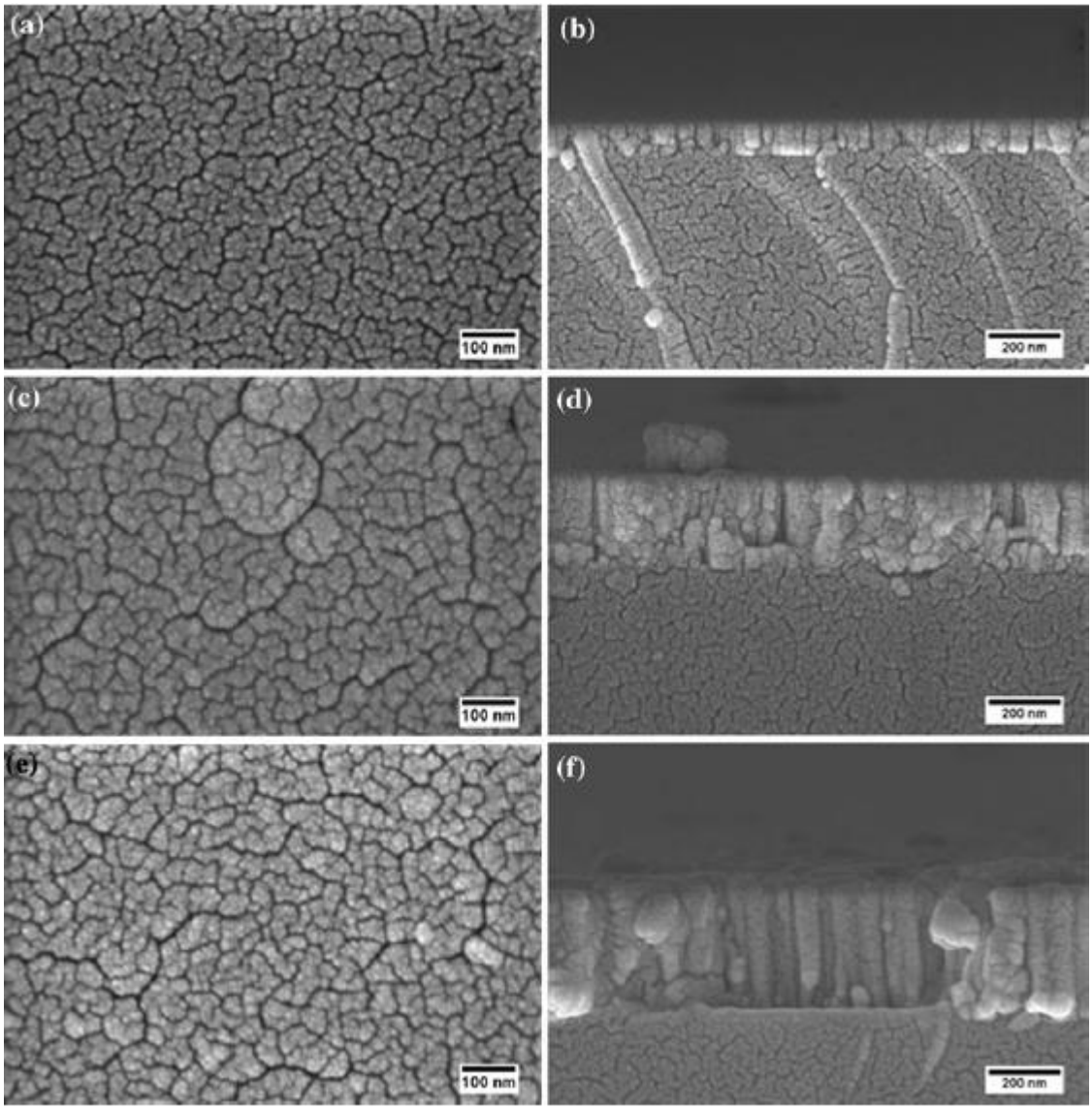

Figure A3: Planar as well as cross-sectional image of nickel deposited at 50W (images a & b), 200W (images c & d), 300 (images e & f)

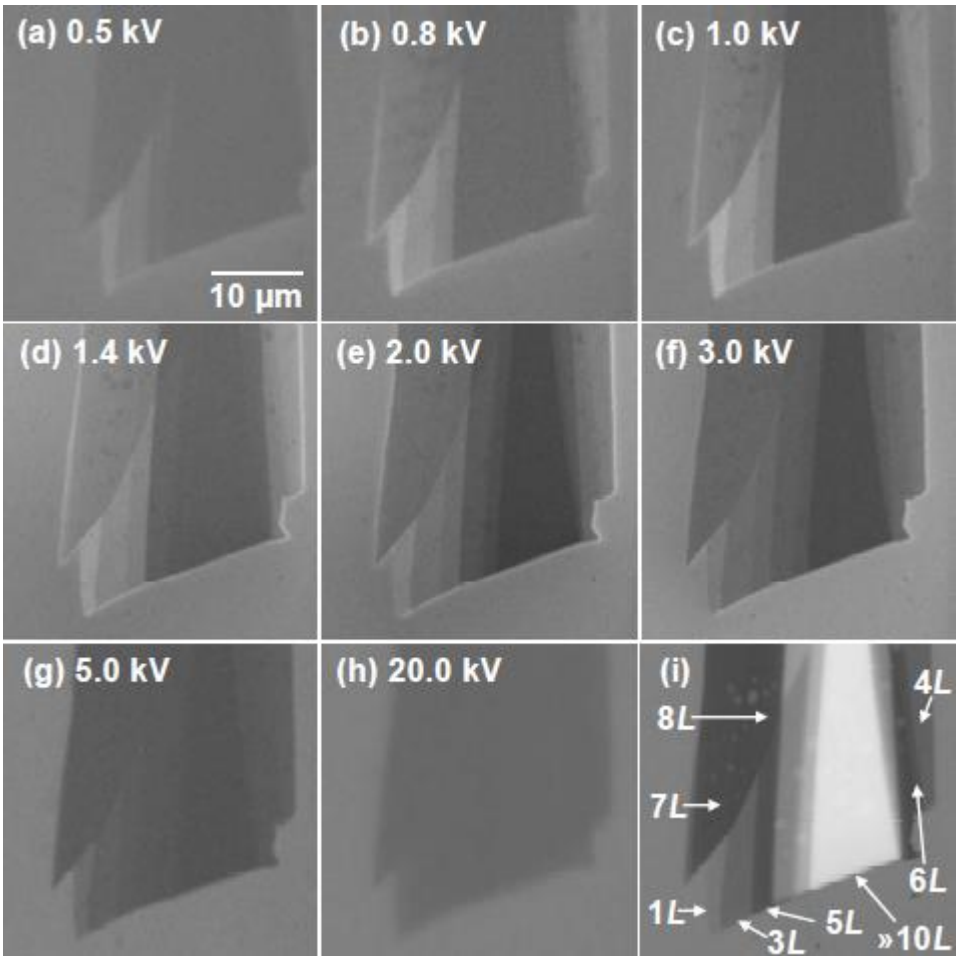

Figure A4: Various layers of graphene observed using SEM at specific primary electron acceleration voltage.

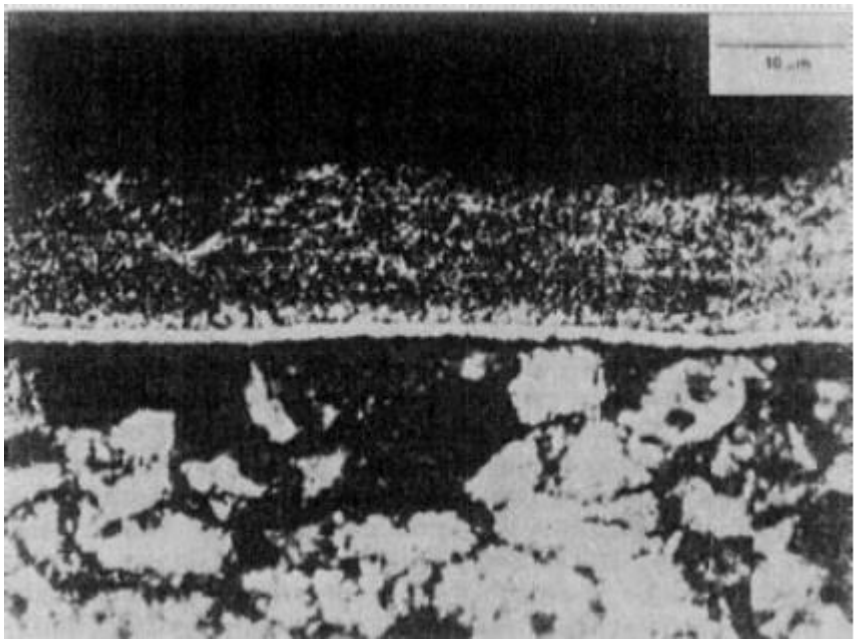

Figure A5: Depiction of an intermetallic layer after Ni-P is deposited on steel.

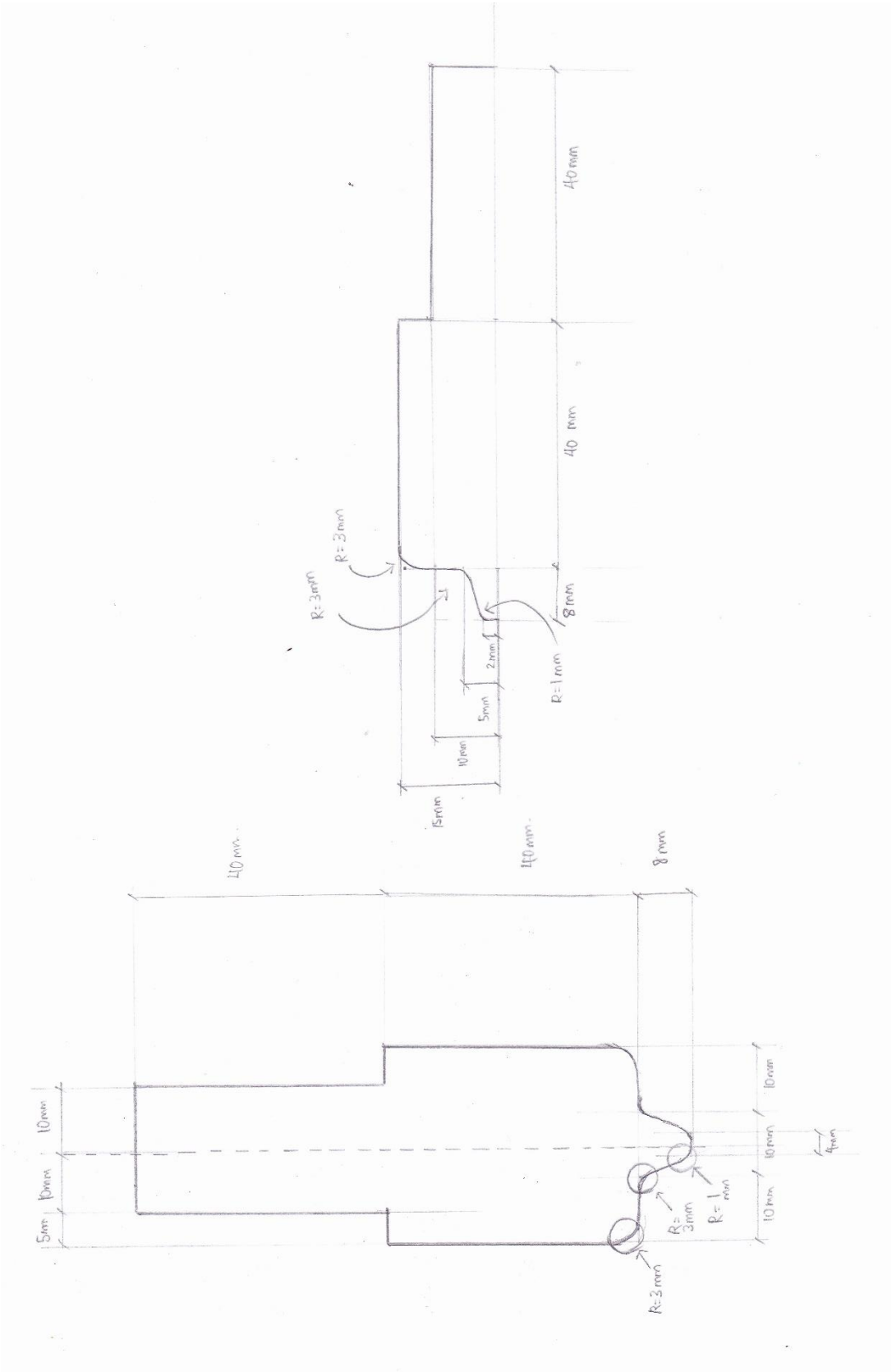

Figure A6: Rough sketch of simple FSW tool.